Geophysical Research Letters

RESEARCH LETTER
10.1029/2021GL096527

Thirty Years of GOSHIP and WOCE Data: Atlantic Overturning of Mass, Heat, and Freshwater Transport

V. Caínzos[1], A. Hernández-Guerra[1], G. D. McCarthy[2], E. L. McDonagh[3,4], M. Cubas Armas[1], and M. D. Pérez-Hernández[1]

[1]Unidad Océano y Clima, Instituto de Oceanografía y Cambio Global, IOCAG, Universidad de Las Palmas de Gran Canaria, ULPGC, Unidad Asociada ULPGC-CSIC, Canary Islands, Spain, [2]ICARUS, Department of Geography, Maynooth University, Maynooth, Ireland, [3]NORCE Norwegian Research Centre, Bjerknes Centre for Climate Research, Bergen, Norway, [4]National Oceanography Centre (NOC), Southampton, UK

Key Points:

- No changes at any latitude between hydrographic sections carried out in the last 30 years
- The major contributor to the Atlantic Meridional Overturning Circulation at the subpolar North Atlantic is the Eastern subbasin for the three decades
- The increase of southward freshwater overturning transport at 30°S indicates a bistable state of the AMOC

Supporting Information:

Supporting Information may be found in the online version of this article.

Correspondence to:

V. Caínzos,
veronica.cainzos@ulpgc.es

Citation:

Caínzos, V., Hernández-Guerra, A., McCarthy, G. D., McDonagh, E. L., Cubas Armas, M., & Pérez-Hernández, M. D. (2022). Thirty years of GOSHIP and WOCE data: Atlantic overturning of mass, heat, and freshwater transport. *Geophysical Research Letters*, *49*, e2021GL096527. https://doi.org/10.1029/2021GL096527

Received 13 OCT 2021
Accepted 31 JAN 2022

Abstract The Atlantic Meridional Overturning Circulation (AMOC) plays a vital role in global climate, redistributing heat, and freshwater. It is predicted to decline due to anthropogenic climate change, with major implications for global climate. Accurately assessing AMOC strength with in situ observations has inspired a number of dedicated observing systems in the Atlantic since the 2000s. However, no consensus has been reached on whether the slowdown of the AMOC and its associated heat and freshwater transports is occurring. These dedicated systems are too recent to detect long-term trends. We have analyzed hydrographic data from zonal sections across the Atlantic for 30 years that predate and overlap the era of AMOC observations. Our results show no changes in the AMOC for all sections analyzed over the whole Atlantic for the last 30 years. We also find an increased export of freshwater from the South Atlantic associated with an increase in upper salinity.

Plain Language Summary The Atlantic Meridional Overturning Circulation (AMOC) is the oceanic process by which upper warm waters flow northward and cold deep waters flow southward. The AMOC has a large effect on European and global climate. Models have predicted a decline of its strength due to anthropogenic climate change. Across-ocean systems monitoring the currents on the water column have yet to find this slowdown. We have analyzed hydrographic data collected for the last 30 years and have built a model for each decade of the circulation of the Atlantic, and found no changes in time in the Atlantic Ocean for each hydrographic section. Also, our results present an increase in the amount of freshwater leaving the South Atlantic.

1. Introduction

The Atlantic Meridional Overturning Circulation (AMOC) transports relatively warm surface, thermocline, and intermediate waters northwards. This warm upper limb of the overturning circulation releases heat to the atmosphere on its way northward, loses buoyancy, and eventually sinks in the subpolar North Atlantic (SPNA) and Nordic Seas, returning south as North Atlantic Deep Water (NADW; Srokosz et al., 2012). Recent publications have addressed the long-term millennial evolution of the AMOC and suggest that it has been in a relative weak state in recent decades (Caesar et al., 2021). AMOC also varies on timescales from seasonal to decadal (Desbruyères et al., 2019; Moat et al., 2020; Sévellec & Sinha, 2018).

A great effort to sample the global ocean has been carried out since the 1990s under the World Ocean Circulation Experiment (WOCE) and, later, the GO-SHIP (Talley et al., 2016) programs. As a result, a global network of zonal and meridional transoceanic hydrographic sections is available, with repetitions every 5–10 years. The WOCE hydrographic cruises enabled the computation of a global ocean linear inverse box model for the 1990s focused on estimating the transports of mass, heat, and freshwater in every ocean (Ganachaud & Wunsch, 2000, 2003), thus creating a consistent picture of the global ocean circulation.

The need for further information about the evolution of the AMOC led to the deployment of several mooring arrays in key latitudes to continuously measure the AMOC. The OSNAP (Lozier et al., 2017), RAPID/MOCHA/WBTS array (hereafter the RAPID array; Cunningham et al., 2007; Johns et al., 2011), MOVE (Kanzow et al., 2006), TSAA (Hummels et al., 2015), and SAMBA (Meinen et al., 2013) projects in the Atlantic Ocean have measured the overturning transport variability on timescales of days, months, or seasons (Frajka-Williams et al., 2019; McCarthy et al., 2020). However, with the earliest results dating the 2000s, these mooring arrays

cannot address the longer term decadal changes in the Atlantic Ocean. Hydrographic data, therefore, offer the only opportunity to understand longer term subsurface variability. Thus, different studies have compared hydrographic sections conducted at different times, to determine changes of these transports at selected latitudes (Baringer & Molinari, 1999; Bryden et al., 2005; Fu et al., 2018; Hernández-Guerra & Talley, 2016; Hernández-Guerra et al., 2014, 2019; Koltermann et al., 1999; McDonagh et al., 2015).

2. Materials and Methods

We have constructed three inverse models in a neutral density (Jackett & McDougall, 1997) framework, one for each of the last three decades, using hydrographic data for the entire Atlantic Ocean. The latitudinal configuration in each decade varies depending on the available transoceanic sections.

2.1. Hydrographic Data

Basinwide, zonal sections, collected since the 1990s, are part of a collective effort to characterize the ocean in the frame of the international GO-SHIP Program (Talley et al., 2016).

We have prioritized the repeated zonal sections for each decade in our study (Figure 1), which are: 55°N (AR07W + AR07E), 24°N (A05), and 30°S (A10). Table S1 in Supporting Information S1 summarizes the chosen sections and their characteristics.

Atlantic water masses are identified with potential temperature, salinity, and neutral density (γ^n) vertical sections (Figure S1 in Supporting Information S1), which allow defining the reference layer for each section to be used in the thermal wind equation to estimate the geostrophic velocities and transports. The level of no motion is set at the interphase of water masses with different directions, such as the southward NADW and the northward Antarctic Bottom Water (AABW). To compute the mass transports, the water column is divided into several γ^n layers (Hernández-Guerra et al., 2019; Talley, 2008). Additionally, the surface Ekman transport at the time of the cruise is estimated using the NCEP–NCAR surface winds.

2.2. Inverse Box Model

The estimated mass transport is not balanced with its adjacent hydrographic sections, as the assumed level of no motion has indeed a velocity different from zero. Thus, inverse box models were introduced in oceanography to estimate the unknown geostrophic reference velocities for hydrographic station pairs, subject to chosen constraints and uncertainties, the most basic of which is mass conservation (Wunsch, 1978, 1996). Conservation of mass is imposed for each box for the whole water column and each layer. For every single section, mass is conserved for regional constraints, related to independent in situ measurements and topographic features. The salinity content of each section is also constrained (Tables S3, S4 and S5 in Supporting Information S1) to make sure that mass is conserved while allowing changes in freshwater. The Gauss-Markov estimator is applied to solve these matrices (Wunsch, 1996). The same model configuration is used for each decade, so that differences in the model solution are attributable to changes in circulation.

3. Results and Discussion

3.1. Meridional Transport

Two counter-rotating overturning cells appear in the results of the inverse models (background arrows in Figure 2). The upper overturning cell is partially closed by the vertical transport of water, with downward vertical transport in the SPNA associated with entrainment of warm North Atlantic Current (NAC; McCartney & Talley, 1984) and upwelling in the subtropical gyre of the South Atlantic Ocean (Figure 2). In the abyssal cell, part of the southward flowing NADW sinks in the Southern Ocean and then returns northward as the AABW (Wefer et al., 1996) that then upwells on its way north to the subtropical North Atlantic. This study does not reach latitudes south enough to observe the deep-water formation in the Southern Ocean. The northward transports of upper and abyssal layers are balanced by the southward transport of deep layers (Kersalé et al., 2020). The boundaries of the deep layers lie between γ^n of 27.84 and 28.15 kg m^{-3} for the southern hemisphere and between or 27.58 and 28.15 kg m^{-3} or bottom for the northern hemisphere.

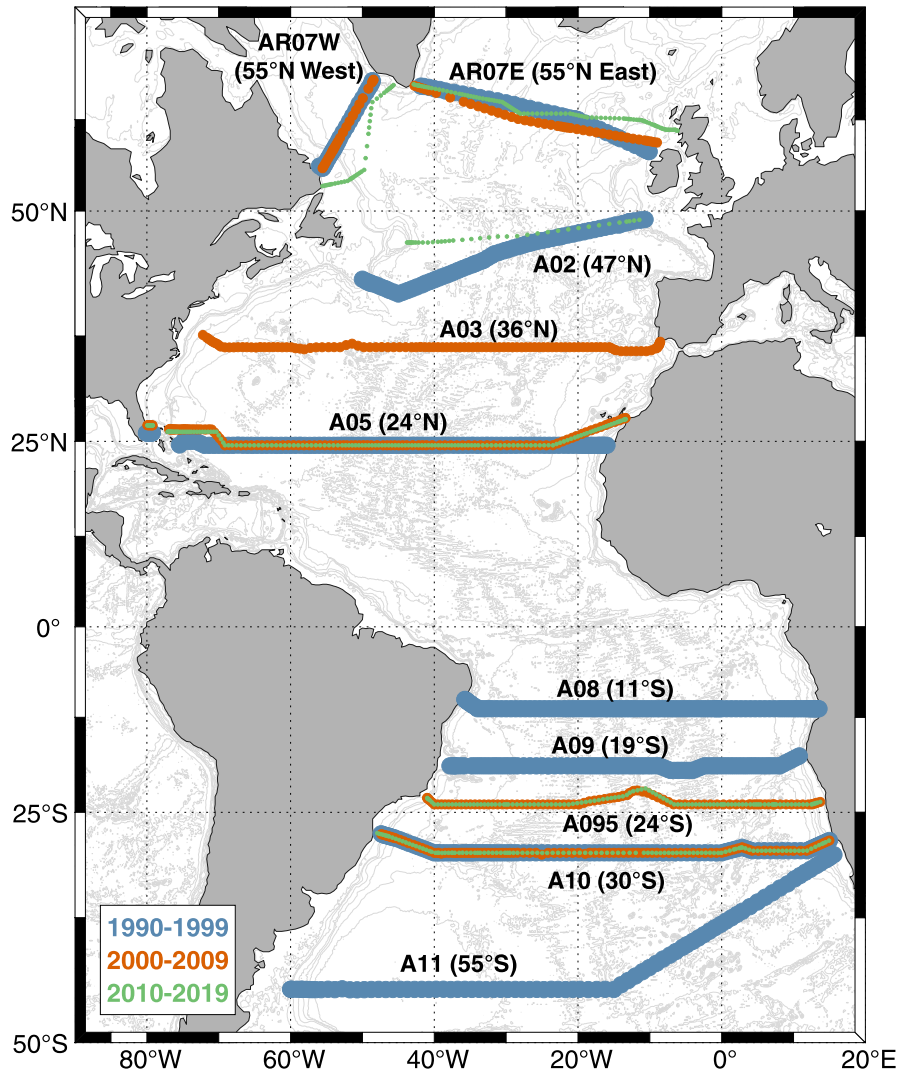

Figure 1. Map of the zonal sections included in each decade for the inverse model. Each section is accompanied by its World Ocean Circulation Experiment name and its nominal latitude (between parenthesis) and the colors represent each decade, blue for 1990–1999, orange for 2000–2009, and green for 2010–2019. Three sections have been repeated in every decade (A10 – 30°S, A05 – 24°N, AR07W and AR07E – 55°N).

In the SPNA, the core of the warm NAC gets denser on its way northward, as seen in sections 47°N and 55°N (Figure 2), with stronger northward transports between γ^n of 26.45 and 27.58 kg m^{-3} at 47°N (12.4 ± 1.8 Sv for 1990–1999 and 13.7 ± 1.5 Sv for 2010–2019) and between γ^n of 27.23 and 27.84 kg m^{-3} at 55°N (12.1 ± 2.5 Sv for 1990–1999, 11.0 ± 1.9 Sv for 2000–2009 and 11.6 ± 1.7 Sv for 2010–2019, where 1 Sverdrup (Sv) = 10^6 m^3 s^{-1} ≈ 10^9 kg s^{-1}). This maximum is associated with stronger downwelling values at 27.00–27.84 kg m^{-3}.

In the thermocline layers of the subtropical regions of both hemispheres (sections 24°S, 19°S, 11°S, 24°N and 36°N) the transport is maximum at the surface, decreasing with depth, reflecting the usual structure of a wind-driven subtropical gyre. The apparent variability in the horizontal and vertical fluxes observed in Figure 2 could be due to the different latitudinal extent among sections in the different decades.

3.2. Overturning Circulation

The meridional overturning circulation is evident in the section-average net transport of northward water by the upper and abyssal layers and by the southward transport by deep layers for all latitudes (Figure 3).

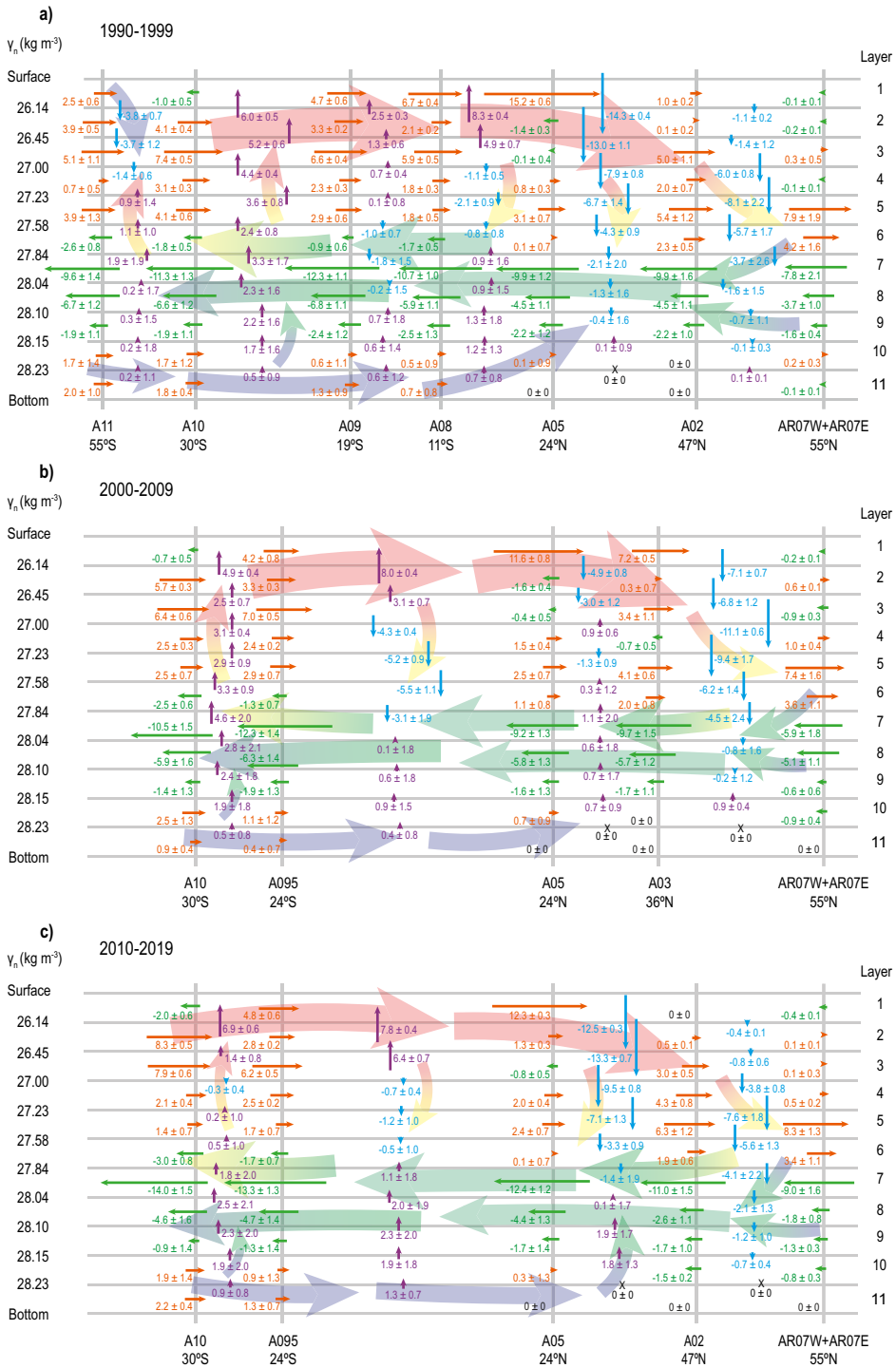

Figure 2. Vertical and meridional schematic of the circulation in the Atlantic Ocean for each decade. The gray horizontal lines mark the neutral density interphases, and the gray vertical lines are the position of each zonal section at their nominal latitude for the (a) 1990–1999 decade, (b) 2000–2009 decade, and (c) 2010–2019 decade. The horizontal mass transport (1 Sverdrup (Sv) = 10^6 m^3 s^{-1} ≈ 10^9 kg s^{-1}) is represented with horizontal arrows, in orange for northward (positive) transport and green for southward (negative) transport. Black dots in the North Atlantic appear in layers with null transport. The vertical transport between two sections in the interphase between two layers is represented with vertical arrows, in violet for upward (positive) transport and blue for downward (negative) transport. Black crosses represent layers with no vertical transport. The uncertainties associated with mass transport are part of the results of the inverse model using the Gauss-Markov estimator. Background arrows manifest the presence of two counter-rotating overturning cells across the basin. A consistent circulation through the decades is observed, with upwelling in the southern subtropical gyre and downwelling in the northern subtropical gyre and the subpolar North Atlantic.

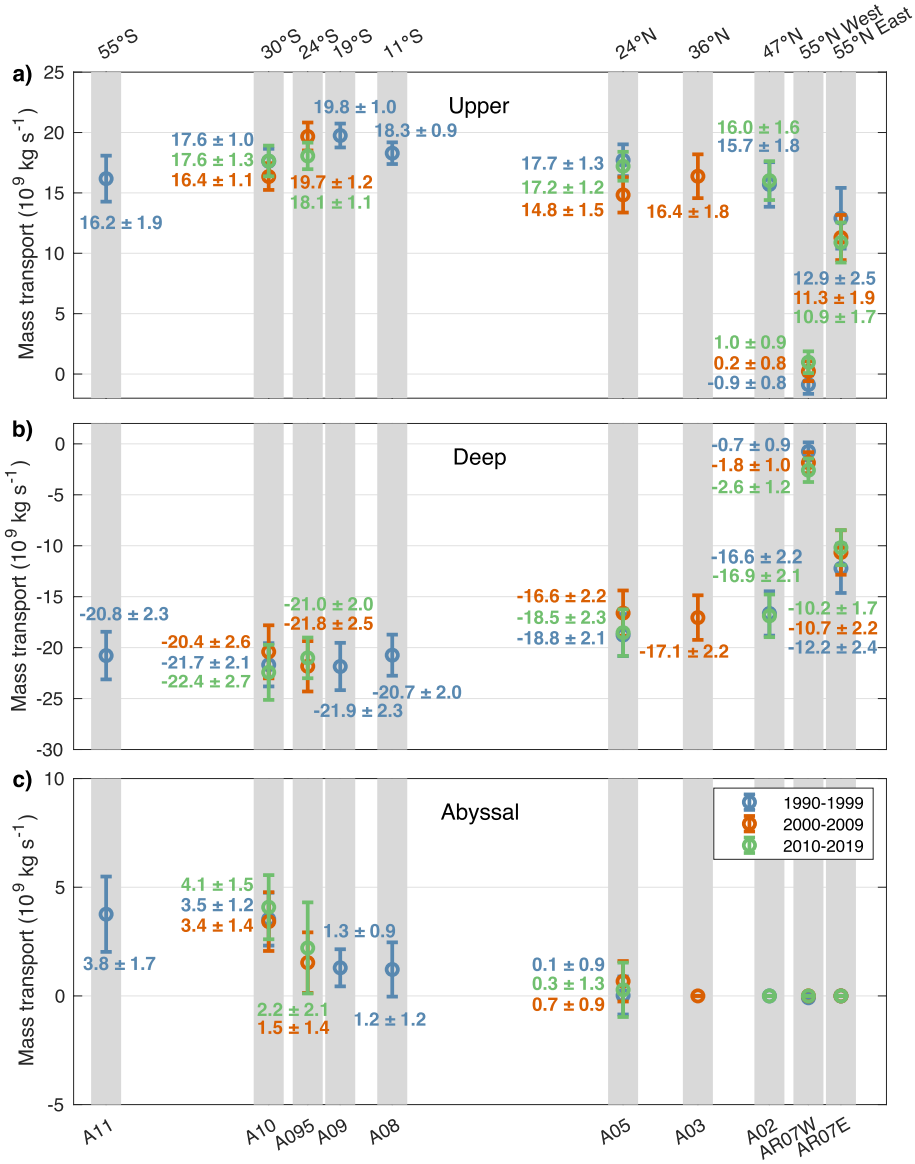

Figure 3. Mass transport (1 Sverdrup (Sv) = 10^6 m^3 s^{-1} ≈ 10^9 kg s^{-1}) attending to each layer for each latitude and decade. The gray bars mark the nominal latitude of each zonal section, and the colors represent each decade, blue for 1990–1999, orange for 2000–2009, and green for 2010–2019. The mass transport is divided into three layers – upper (a), deep (b), and abyssal (c). The interphases between these layers are defined as the change from north to south (south to north) transport for upper to deep (deep to bottom) layers in neutral density coordinates. The uncertainties associated with the mass transport are part of the results of the inverse model solved using the Gauss-Markov estimator.

There is no apparent change in the overturning strength among the diverse hydrographic realizations carried out in different decades, with no differences for the upper, deep, and abyssal layers across the Atlantic Ocean. However, we have to be aware that there are some limitations associated with inverse modeling of hydrographic data. Each inverse solution could be interpreted as representative of a relatively short time interval (Fu et al., 2020) or could give information of monthly variations of the AMOC (Bryden et al., 2005). Similarly, Ganachaud and Wunsch (2003) refer to their estimates as time-average transoceanic transports with realistic uncertainties, although they acknowledge the temporal sampling problem inherent to the discrete sampling of hydrographic data.

Our results are similar to those obtained by other inverse models of the Atlantic with data of the first decade of our study (Ganachaud, 2003b; Lumpkin & Speer, 2007; Macdonald, 1995; Sloyan & Rintoul, 2001; Table S2 in Supporting Information S1). In general, the results agree, but we find more differences in upper layers and our model

tends to provide smaller transports in bottom layers. A recent reconstruction of three decades of inverse models using sections north of 24°N (Fu et al., 2020) has also found stability in the strength of the AMOC for the SPNA.

OSNAP data products are available for 21 months, from July 2014 to March 2016 (Lozier et al., 2019). AMOC values from OSNAP data can be compared to those of the inverse model for the last decade of the section at 55°N (West and East) but taking into account the shorter period in OSNAP data and the limitation of the inverse model solutions described before. The mass transports from the inverse model for each subbasin (1.0 ± 0.9 Sv for the West and 10.9 ± 1.7 Sv for the East) are slightly weaker than those obtained by OSNAP (2.1 ± 0.3 Sv for the West and 15.6 ± 0.8 Sv for the East). However, for the total section, the subpolar AMOC is not different (11.9 ± 2.1 Sv for the inverse model and 14.9 ± 0.9 Sv for OSNAP). Our results indicate a fairly constant weak transport in the Labrador basin over the three decades, and the Eastern basin being the major contributor to the AMOC, evidencing the OSNAP findings (Lozier et al., 2019; Petit et al., 2020) of weak transport in the Labrador Sea between 2014 and 2016 that have persisted for the previous three decades.

AMOC estimates are also available for the RAPID program from April 2004 to August 2018 (Moat et al., 2020). Values for the 2010–2019 decade are very similar between the inverse model (24°N cruise in 2011) and RAPID (over 2010–2018) for upper (17.2 ± 1.2 and 16.4 ± 4.5 Sv, respectively), deep (-18.5 ± 2.3 and -17.3 ± 4.1 Sv, respectively) and abyssal (0.3 ± 1.3 and 1.1 ± 0.6 Sv, respectively) layers. The mass transports of the inverse model of the 2000-2009 decade (24°N cruise in 2004) are weaker than RAPID values (averaged over the interval 2004–2009) for upper (14.8 ± 1.5 and 18.0 ± 4.7 Sv, respectively), deep (-16.6 ± 2.2 and -18.6 ± 4.3 Sv, respectively), and abyssal (0.7 ± 0.9 and 0.8 ± 0.6 Sv, respectively), although not different, in part due to the high uncertainties associated to RAPID data.

The question of the slowing of the AMOC or not is exceptionally important. Contrasting the results of in situ observations and reconstructions is a significant contribution to the debate. Monitoring programs enabled the observation of interannual changes in AMOC, such as the 0.5 Sv/year weakening of the AMOC at 26.5°N between 2004 and 2012, possibly explained by internal variability (Roberts et al., 2014), although recent studies using empirical analysis of hydrographic RAPID data dating back to the 1980s show no overall decline (Worthington et al., 2021). Other higher-frequency variations can be found, such as the ∼30% 2009–2010 decrease of AMOC at 26.5°N based on the previous 5 years of measurements (McCarthy et al., 2012). This decrease in strength was detected in the AMOC upper limb at 41°N but not in the deep western return limb at 16°N (MSrokosz & Bryden, 2015; Srokosz et al., 2012).

The relationship between temperature and AMOC enables the use of satellite sea surface temperature as a proxy for long-term reconstructions of AMOC strength (Caesar et al., 2018; Manta et al., 2021), which can be compared to the estimations obtained with global climate numerical models (Caesar et al., 2018; Fraser & Cunningham, 2021). Longer term reconstructions and projections from proxies and high-resolution climate models display a decline in the strength of the AMOC by 15% (Caesar et al., 2018) and 30% (Rahmstorf et al., 2015) since the 1950s, in the frame of a consistent weak AMOC for the last 150 years (Thornalley et al., 2018). Fraser and Cunningham (2021) have found no significant weakening trend in their reconstruction of AMOC over the last 120 years. Expendable bathythermograph (XBT) and Argo profile data enable the estimation of AMOC (Goes et al., 2020; Majumder et al., 2016), and results agree with our inverse model, especially for XBT-derived solutions, with Argo estimates being considerably higher. Monthly XBT transects could complement the study of short-term variability of the AMOC.

3.3. Heat Transport

Total heat transport can be divided into its components attending to the mechanisms of vertical and horizontal circulation, allowing to break up the heat transport into a barotropic (throughflow), baroclinic (overturning), and horizontal (or gyre) component (Bryden & Imawaki, 2001). The throughflow component is the net transport across the section at the section-averaged temperature (Figure S2 in Supporting Information S1); the overturning component is the zonally averaged vertical circulation and the horizontal or gyre component is the horizontal and vertical residual heat (Bryden & Imawaki, 2001; Bryden et al., 2011; McDonagh et al., 2015; Figures 4a, 4c and 4e). Overall, the overturning heat transport (Figure 4c), which represents changes in the meridional structure of the water column, dominates the total heat transport and increases equatorward. The horizontal or gyre

component (Figure 4e) comprises the result of large-scale gyre circulation and eddies, which remains fairly constant across all latitudes and through the decades of this study (McDonagh et al., 2015).

The North Atlantic subtropical gyre (24°N) shows a greater change in terms of overturning heat transport than in the rest of sections, with a strong decrease from a maximum value in 1990–1999 of 1.27 ± 0.06 PW to 0.97 ± 0.07 in 2000–2009 PW and a recovery to 1.10 ± 0.05 PW in 2010–2019. The Labrador Sea (55°N West) net transports are almost null, with negligible contributions from the marked cyclonic gyre affecting the whole basin (Lozier et al., 2019), vertically and horizontally. Nevertheless, in the Eastern subbasin of the northernmost section (55°N East) the overturning component majorly contributes to the total heat transport.

3.4. Freshwater Transport

Oceanic freshwater transport is the non-salt part of mass transport. Its divergence can be understood as the balance of evaporation, precipitation, river runoff, and ice processes. It is calculated by constraining the salt flux across each section to that across the Bering Strait. The salt flux (or non-freshwater part of the mass transport) is not affected by the strength of freshwater divergence as this happens at zero salinity. The freshwater divergence (Figures 4b, 4d and 4f) can be divided, as the heat transport, into its components. On this occasion and in contrast to the heat flux, the freshwater throughflow contributes from 5% to 35% to the total flux (Figure S2 in Supporting Information S1). This component represents the evolution of the section average salinity from that of the Bering Strait (a southward flow of 0.8 Sv with an average salinity of 32.5, resulting in a salinity flux of −26.0 Sv psu; McDonagh & King, 2005; Woodgate & Aagaard, 2005). The freshwater overturning component (Figure 4d) presents a stronger southward transport in the sections close to the equator. The horizontal or gyre freshwater flux (Figure 4f) displays a higher northward freshwater flux in the sections that occupy the subtropical gyres (24 and 36°N in the North Atlantic and 24 and 30°S in the South Atlantic), with similar values for all decades.

The south Atlantic subtropical gyre presents low values of overturning freshwater flux at 30°S, thus being the only section with a horizontal component larger than the overturning (Mecking et al., 2016). Based on our understanding from model studies, the overturning freshwater flux at this latitude has been identified as a possible proxy for the stability of the AMOC (Bryden et al., 2011; De Vries & Weber, 2005; Dijkstra, 2007; Gent, 2018; Rahmstorf, 1996; Weber & Drijfhout, 2007; Weijer et al., 2019), potentially determining whether it is in a monostable or bistable regime. We have found a tendency toward increasingly southward values from 1990 to 1999 (0.00 ± 0.02 Sv) to 2000–2009 (−0.08 ± 0.02 Sv), and no differences within uncertainties between the 2000–2009 decade and the 2010–2019 decade (−0.13 ± 0.03 Sv), with an overall change between 1990–1999 and 2010–2019. Negative values of the overturning freshwater transport at 30°S indicate that the AMOC transports freshwater southwards, and a net input of freshwater north of 30°S is necessary to maintain the salinity structure of the overturning circulation. This result is consistent with other studies relying on observational data that have found that the overturning circulation effectively carries freshwater out of the Atlantic through its southern boundary (Bryden et al., 2011; Garzoli et al., 2013; McDonagh & King, 2005; Saunders & King, 1995; Weijer et al., 1999).

The transport weighted sensitivity of the overturning and horizontal components reflects the change in each component subtracting the effect of a change in the mass transport. The transport weighted freshwater overturning—the freshwater overturning divided by the overturning strength— at 30°S shows a systematic decrease (0.000 ± 0.001, −0.005 ± 0.001, and −0.008 ± 0.002 for each hydrographic cruise done in each decade, respectively) that reflects an increasing difference between the freshwater content in upper and lower layers. To assess the origin of this change, we have computed the transport and area-weighted salinity for upper and thermocline, intermediate, and deep layers. The area-weighted salinity (Figure 4g) values for each layer fail to show changes for each decade. However, the transport-weighted salinity (Figure 4h) for upper and thermocline layers presents higher variability (34.45, 34.68, and 34.96 for the realizations carried out in each decade), whereas the intermediate and deep layers remain fairly constant. Thus, this change in the freshwater overturning arises from an increase in the salinity of upper layers transported northward in the upper ocean, possibly due to higher transport of the salty waters of the Agulhas leakage from the Indian Ocean. Model simulations have indicated that there might be a Southern Hemisphere origin to the AMOC decadal variability arising from the Agulhas leakage (Biastoch et al., 2008). The strength of this variability factor decreases northward but can reach up to 0.6 Sv. On longer timescales, it has shown a correlation with the Atlantic Multidecadal Oscillation, and it has been linked

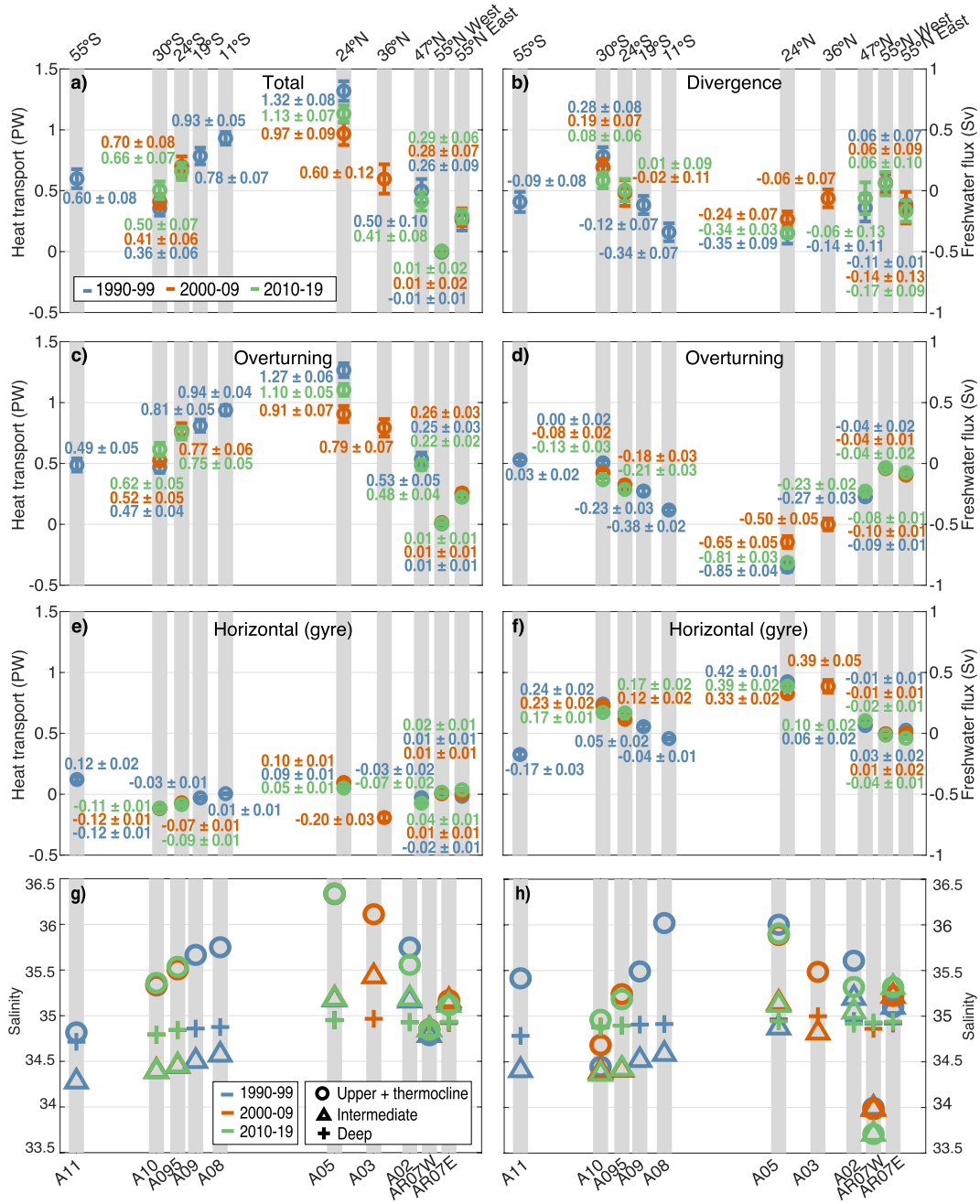

Figure 4. Heat and freshwater transport attending to their components, and area and transport-weighted salinity for each latitude and decade. The gray bars mark the nominal latitude of each zonal section, and the colors represent each decade, blue for 1990–1999, orange for 2000–2009, and green for 2010–2019. The left panels (a, c, and e) are the heat transport in PW, and the panels on the right (b, d, and f) are the freshwater transport in Sv. The total transport (a) and (b) is divided in throughflow, overturning (c) and (d), and horizontal or gyre (e) and (f). The total heat transport (a) is similar to the overturning heat transport (c), as the horizontal component (e) is quite small. The freshwater divergence (b) also looks like the overturning component (d), but the horizontal (f) component cannot be neglected. The higher variability among decades appears at 24°N in both property fluxes for the overturning component. There is an increase in northward heat transport and southward freshwater transport equatorward. The uncertainties associated with the heat and freshwater transports are part of the results of the inverse model solved using the Gauss-Markov estimator. The bottom panels are the area-weighted (g) and transport-weighted salinity (h). Each property has been divided into three water masses – upper and thermocline waters (circles), intermediate waters (triangles), and deep waters (crosses). The area-weighted salinity (g) does not show any decadal changes for any water masses, although the transport-weighted salinity (h) manifests an increasing trend at 30°S for the upper and thermocline waters. As a result, the stratification in the water column is stronger, reflected in the higher values of the overturning component of freshwater.

to wind-driven processes (Biastoch et al., 2015). Other studies have found no significant impact on the AMOC (Weijer & van Sebille, 2014), and therefore, a discussion on this topic continues.

4. Conclusions

The behavior of the AMOC and its driving mechanisms and feedbacks have received much attention in climate change scenarios due to the major climate impacts associated with a predicted slowdown. As a result, several ocean locations are being monitored to estimate the changes in the strength of the AMOC at different latitudes.

Our results from inverse models based on hydrographic data show that the Atlantic basin overturning transport displays no changes at any latitude between the different hydrographic cruises. In the SPNA, our results indicate that the major contributor to the AMOC for the three decades is the Eastern basin (55°N East) as estimated by OSNAP for the last decade.

At 30°S, an increase of southward freshwater overturning transport has been estimated over the three decades, indicating that the AMOC is possibly in a bistable state based on findings from model studies. These negative values appear when AMOC exports freshwater out of the Atlantic, equivalent to a net precipitation over the Atlantic basin. In this case, the AMOC has multiple equilibria and may collapse due to a large enough freshwater perturbation (Dijkstra, 2007; Mecking et al., 2016; Weijer et al., 2019).

Data Availability Statement

Hydrographic data were collected from the CCHDO website (https://cchdo.ucsd.edu) in the frame of International WOCE and GO-SHIP projects and from the BODC databases for each cruise: A11 1992 (https://cchdo.ucsd.edu/cruise/74DI199_1), A10 1992 (https://cchdo.ucsd.edu/cruise/06MT22_5), A09 1991 (https://cchdo.ucsd.edu/cruise/06MT15_3), A08 1994 (https://cchdo.ucsd.edu/cruise/06MT28_1), A05 1992 (https://cchdo.ucsd.edu/cruise/29HE06_1), A02 1993 (https://cchdo.ucsd.edu/cruise/06GA226_2), AR07 W 1990 (https://cchdo.ucsd.edu/cruise/18DA90012_1), AR07 E 1991 (https://cchdo.ucsd.edu/cruise/74AB62_1), A10 2003 (https://cchdo.ucsd.edu/cruise/49NZ20031106), A095 2009 (https://cchdo.ucsd.edu/cruise/740H20090307), A05 2004 (https://cchdo.ucsd.edu/cruise/74DI20040404), A03 2005 (https://www.bodc.ac.uk/data/bodc_database/ctd/search/, searching for 36 North under 'Project'), AR07 W 2005 (https://cchdo.ucsd.edu/cruise/18HU20050526), AR07 E 2007 (https://cchdo.ucsd.edu/cruise/64PE20070830), A10 2011 (https://cchdo.ucsd.edu/cruise/33RO20110926), A095 2018 (https://cchdo.ucsd.edu/cruise/740H20180228), A05 2011 (https://cchdo.ucsd.edu/cruise/29AH20110128), A02 2013 (https://cchdo.ucsd.edu/cruise/06M220130509), AR07 W 2014 (https://cchdo.ucsd.edu/cruise/74JC20140606) and AR07 E 2014 (https://cchdo.ucsd.edu/cruise/74JC20140606). OSNAP data were collected and made freely available by the OSNAP project and all the national programs that contribute to it (https://www.o-snap.org/). Data from the full OSNAP array for the first 21 months (31-Jul-2014 to 20-Apr-2016) have been used to produce the 30-day mean MOC, MHT, and MFT time series across the whole section, as well as the gridded property fields, and are available at https://doi.org/10.35090/wa93-m688. Data from the RAPID-MOCHA program are funded by the U.S. National Science Foundation and UK Natural Environment Research Council. MOC data from the RAPID-MOCHA are freely available at https://rapid.ac.uk/rapidmoc/rapid_data/datadl.php (doi:10/d3z4) and heat transports at https://mocha.rsmas.miami.edu/mocha/results/index.html (doi:10/gwqg). The Florida Current cable and section data are made freely available on the Atlantic Oceanographic and Meteorological Laboratory web page (www.aoml.noaa.gov/phod/floridacurrent/) and are funded by the DOC-NOAA Climate Program Office - Ocean Observing and Monitoring Division. Florida Current daily mean transport from year 2000 until present is available at https://www.aoml.noaa.gov/phod/floridacurrent/data_access.php and historical data from 1982 to 1998 at https://www.aoml.noaa.gov/phod/floridacurrent/historical_data.php, of which we have used the used data from 1990 to 1998. The daily mean u and v-wind components of NCEP/NCAR reanalysis winds were collected from https://psl.noaa.gov/data/gridded/data.ncep.reanalysis.pressure.html.

Acknowledgments
We thank the chief scientists and teams that collected all the data for the zonal sections: P. Saunders, T. Müller, G. Siedler, G. Parrilla, A. Sy, J. Lazier, M. Bersch, Y. Yoshikawa, B. King, S. Cunningham, G. Harrison, G. J.Brummer, M. Baringer, A. Macdonald, D. Kieke, and P. Holliday. This article is a publication of the Unidad Océano y Clima from Universidad de Las Palmas de Gran Canaria, an R&D&i CSIC-associate unit. This work has been completed as part of V.C. work at IOCAG, in the doctoral program in Oceanography and Global Change. V.C. acknowledges the Agencia Canaria de Investigación, Innovación y Sociedad de la Información (ACIISI) grant program of "Apoyo al personal investigador en formación" TESIS2019010015, as well as NORCE for hosting a guest student to develop the study. M.D.P.-H. would like to thank the support of the "Programa Postdoctoral de la Universidad de Las Palmas de Gran Canaria". This study was supported by the SAGA project (RTI2018-100844-B-C31) funded by the Ministerio de Ciencia, Innovación y Universidades of the Spanish Government. This study was additionally supported by the TRIATLAS project, which has received funding from the European Union's Horizon 2020 research and innovation programme under grant agreement No 817578.

References

Baringer, M. O., & Molinari, R. (1999). Atlantic Ocean baroclinic heat flux at 24 to 26°N. *Geophysical Research Letters*, *26*(3), 353–356. https://doi.org/10.1029/1998gl900323

Biastoch, A., Böning, C. W., & Lutjeharms, J. R. E. (2008). Agulhas leakage dynamics affects decadal variability in Atlantic overturning circulation. *Nature*, *456*(7221), 489–492. https://doi.org/10.1038/nature07426

Biastoch, A., Durgadoo, J. V., Morrison, A. K., van Sebille, E., Weijer, W., & Griffies, S. M. (2015). Atlantic multi-decadal oscillation covaries with Agulhas leakage. *Nature Communications*, *6*(1), 10082. https://doi.org/10.1038/ncomms10082

Bryden, H. L., & Imawaki, S. (2001). Chapter 6.1 Ocean heat transport. In G. Siedler, J. Church, & J. Gould (Eds.), *ocean circulation & climate: Observing and modelling the global ocean* (pp. 455–474). Academic Press. https://doi.org/10.1016/S0074-6142(01)80134-0

Bryden, H. L., King, B. A., & McCarthy, G. D. (2011). South Atlantic overturning circulation at 24°S. *Journal of Marine Research*, *69*(1), 39–55. https://doi.org/10.1357/002224011798147633

Bryden, H. L., Longworth, H. R., & Cunningham, S. A. (2005). Slowing of the Atlantic meridional overturning circulation at 25°N. *Nature*, *438*, 655–657. https://doi.org/10.1038/nature04385

Caesar, L., McCarthy, G. D., Thornalley, D. J. R., Cahill, N., & Rahmstorf, S. (2021). Current Atlantic meridional overturning circulation weakest in last millennium. *Nature Geoscience*, *14*(3), 1–120. https://doi.org/10.1038/s41561-021-00699-z

Caesar, L., Rahmstorf, S., Robinson, A., Feulner, G., & Saba, V. (2018). Observed fingerprint of a weakening Atlantic Ocean overturning circulation. *Nature*, *556*(7700), 191–196. https://doi.org/10.1038/s41586-018-0006-5

Cunningham, S. A., Kanzow, T., Rayner, D., Baringer, M. O., Johns, W. E., & Marotzke, J. (2007). Temporal variability of the Atlantic meridional overturning circulation at 26.5°N. *Science*, *317*, 935–938. https://doi.org/10.1126/science.1141304

de Vries, P., & Weber, S. L. (2005). The Atlantic freshwater budget as a diagnostic for the existence of a stable shut down of the meridional overturning circulation. *Geophysical Research Letters*, *32*(9), L09606. https://doi.org/10.1029/2004GL021450

Desbruyères, D. G., Mercier, H., Maze, G., & Daniault, N. (2019). Surface predictor of overturning circulation and heat content change in the subpolar North Atlantic. *Ocean Science*, *15*(3), 809–817. https://doi.org/10.5194/os-15-809-2019

Dijkstra, H. A. (2007). Characterization of the multiple equilibria regime in a global ocean model. *Tellus*, *59A*, 695–705. https://doi.org/10.1111/j.1600-0870.2007.00267.x

Frajka-Williams, E., Ansorge, I. J., Baehr, J., Bryden, H. L., Chidichimo, M. P., Cunningham, S. A., et al. (2019). Atlantic meridional overturning circulation: Observed transport and variability. *Frontiers in Marine Science*, *6*(260). https://doi.org/10.3389/fmars.2019.00260

Fraser, N. J., & Cunningham, S. A. (2021). 120 Years of AMOC variability reconstructed from observations using the Bernoulli inverse. *Geophysical Research Letters*, *48*(18). https://doi.org/10.1029/2021GL093893

Fu, Y., Karstensen, J., & Brandt, P. (2018). Atlantic meridional overturning circulation at 14.5°N in 1989 and 2013 and 24.5°N in 1992 and 2015: Volume, heat, and freshwater transports. *Ocean Science*, 589–616. https://doi.org/10.5194/os-14-589-2018

Fu, Y., Li, F., Karstensen, J., & Wang, C. (2020). A stable Atlantic meridional overturning circulation in a changing North Atlantic ocean since the 1990s. *Science Advances*, *6*(48), eabc7836. https://doi.org/10.1126/sciadv.abc7836

Ganachaud, A. S. (2003b). Large-scale mass transports, water mass formation, and diffusivities estimated from World Ocean Circulation Experiment (WOCE) hydrographic data. *Journal of Geophysical Research*, *108*(C7). https://doi.org/10.1029/2002jc001565

Ganachaud, A. S., & Wunsch, C. (2000). Improved estimates of global ocean circulation, heat transport and mixing from hydrographic data. *Nature*, *408*, 453–456. https://doi.org/10.1038/35044048

Ganachaud, A. S., & Wunsch, C. (2003). Large-scale ocean heat and freshwater transports during the world ocean circulation experiment. *Journal of Climate*, *16*, 696–705. https://doi.org/10.1175/1520-0442(2003)016<0696:LSOHAF>2.0.CO;2

Garzoli, S. L., Baringer, M. O., Dong, S., Perez, R. C., & Yao, Q. (2013). South Atlantic meridional fluxes. *Deep-Sea Research Part I Oceanographic Research Papers*, *71*, 21–32. https://doi.org/10.1016/j.dsr.2012.09.003

Gent, P. R. (2018). A commentary on the Atlantic meridional overturning circulation stability in climate models. *Ocean Modelling*, *122*, 57–66. https://doi.org/10.1016/j.ocemod.2017.12.006

Goes, M., Goni, G., Dong, S., Boyer, T., & Baringer, M. (2020). The complementary value of XBT and Argo observations to monitor ocean boundary currents and meridional heat and volume transports: A case study in the Atlantic Ocean. *Journal of Atmospheric and Oceanic Technology*, *37*(12), 2267–2282. https://doi.org/10.1175/JTECH-D-20-0027.1

Hernández-Guerra, A., Pelegrí, J. L., Fraile-Nuez, E., Benítez-Barrios, V. M., Emelianov, M., Pérez-Hernández, M. D., & Vélez-Belchí, P. (2014). Meridional overturning transports at 7.5°N and 24.5°N in the Atlantic Ocean during 1992–93 and 2010–11. *Progress in Oceanography*, *128*, 98–114. https://doi.org/10.1016/j.pocean.2014.08.016

Hernández-Guerra, A., & Talley, L. D. (2016). Meridional overturning transports at 30°S in the Indian and Pacific oceans in 2002–2003 and 2009. *Progress in Oceanography*, *146*, 89–120. https://doi.org/10.1016/j.pocean.2016.06.005

Hernández-Guerra, A., Talley, L. D., Pelegrí, J. L., Vélez-Belchí, P., Baringer, M. O., Macdonald, A. M., & McDonagh, E. L. (2019). The upper, deep, abyssal and overturning circulation in the Atlantic Ocean at 30°S in 2003 and 2011. *Progress in Oceanography*, *176*. https://doi.org/10.1016/j.pocean.2019.102136

Hummels, R., Brandt, P., Dengler, M., Fischer, J., Araujo, M., Veleda, D., & Durgadoo, J. V. (2015). Interannual to decadal changes in the western boundary circulation in the Atlantic at 11°S. *Geophysical Research Letters*, *42*(18), 7615–7622. https://doi.org/10.1002/2015GL065254

Jackett, D. R., & McDougall, T. J. (1997). A neutral density variable for the World's Oceans. *Journal of Physical Oceanography*, *27*(2), 237–263. https://doi.org/10.1175/1520-0485(1997)027<0237:ANDVFT>2.0.CO;2

Johns, W. E., Baringer, M. O., Beal, L. M., Cunningham, S. A., Kanzow, T., Bryden, H. L., et al. (2011). Continuous, array-based estimates of Atlantic Ocean heat transport at 26.5°N. *Journal of Climate*, *24*, 2429–2449. https://doi.org/10.1175/2010JCLI3997.1

Kanzow, T., Send, U., Zenk, W., Chave, A. D., & Rhein, M. (2006). Monitoring the integrated deep meridional flow in the tropical North Atlantic: Long-term performance of a geostrophic array. *Deep-Sea Research Part I Oceanographic Research Papers*, *53*(3), 528–546. https://doi.org/10.1016/j.dsr.2005.12.007

Kersalé, M., Meinen, C. S., Perez, R. C., Le Hénaff, M., Valla, D., Lamont, T., et al. (2020). Highly variable upper and abyssal overturning cells in the South Atlantic. *Science Advances*, *6*(32), eaba7573. https://doi.org/10.1126/sciadv.aba7573

Koltermann, K. P., Sokov, A. V., Tereschenkov, V. P., Dobroliubov, S. A., Lorbacher, K., & Sy, A. (1999). Decadal changes in the thermohaline circulation of the North Atlantic. *Deep-Sea Research Part II Topical Studies in Oceanography*, *46*(1–2), 109–138. https://doi.org/10.1016/S0967-0645(98)00115-5

Lozier, M. S., Bacon, S., Bower, A. S., Cunningham, S. A., de Jong, M. F., Steur, L. de, et al. (2017). Overturning in the subpolar North Atlantic program: A new international Ocean Observing system. *Bulletin of the American Meteorological Society*, *98*(4), 737–752. https://doi.org/10.1175/bams-d-16-0057.1

Lozier, M. S., Li, F., Bacon, S., Bahr, F., Bower, A. S., Cunningham, S. A., et al. (2019). A sea change in our view of overturning in the subpolar North Atlantic. *Science*, *363*(6426), 516–521. https://doi.org/10.1126/science.aau6592

Lumpkin, R., & Speer, K. G. (2007). Global Ocean meridional overturning. *Journal of Physical Oceanography*, *37*(10), 2550–2562. https://doi.org/10.1175/jpo3130.1

Macdonald, A. M. (1995). *Ocean fluxes of mass, heat and freshwater: A global estimate and perspective*. Massachusetts Institute of Technology & Woods Hole Oceanographic Institution. https://doi.org/10.1575/1912/5620

Majumder, S., Schmid, C., & Halliwell, G. (2016). An observations and model-based analysis of meridional transports in the South Atlantic. *Journal of Geophysical Research: Oceans*, *121*. https://doi.org/10.1002/2016jc011693

Manta, G., Speich, S., Karstensen, J., Hummels, R., Kersalé, M., Laxenaire, R., et al. (2021). The South Atlantic meridional overturning circulation and mesoscale eddies in the first GO-SHIP section at 34.5°S. *Journal of Geophysical Research: Oceans*, *126*(2), 1–25. https://doi.org/10.1029/2020JC016962

McCarthy, G., Frajka-Williams, E., Johns, W. E., Baringer, M. O., Meinen, C. S., Bryden, H. L., et al. (2012). Observed interannual variability of the Atlantic meridional overturning circulation at 26.5°N. *Geophysical Research Letters*, *39*, L19609. https://doi.org/10.1029/2012GL052933

McCarthy, G. D., Brown, P. J., Flagg, C. N., Goni, G., Houpert, L., Hughes, C. W., et al. (2020). Sustainable observations of the AMOC: Methodology and technology. *Reviews of Geophysics*, *58*(1), 1–34. https://doi.org/10.1029/2019RG000654

McCartney, M. S., & Talley, L. D. (1984). Warm-to-cold water conversion in the northern North Atlantic Ocean. *Journal of Physical Oceanography*, *14*, 922–935. https://doi.org/10.1175/1520-0485(1984)014<0922:wtcwci>2.0.co;2

McDonagh, E. L., & King, B. A. (2005). Oceanic fluxes in the south Atlantic. *Journal of Physical Oceanography*, *35*(1), 109–122. https://doi.org/10.1175/JPO-2666.1

McDonagh, E. L., King, B. A., Bryden, H. L., Courtois, P., Szuts, Z., Baringer, M. O., et al. (2015). Continuous estimate of Atlantic oceanic freshwater flux at 26.5°N. *Journal of Climate*, *28*, 8888–8906. https://doi.org/10.1175/jcli-d-14-00519.1

Mecking, J. V., Drijfhout, S. S., Jackson, L. C., & Graham, T. (2016). Stable AMOC off state in an eddy-permitting coupled climate model. *Climate Dynamics*, *47*(7–8), 2455–2470. https://doi.org/10.1007/s00382-016-2975-0

Meinen, C. S., Speich, S., Perez, R. C., Dong, S., Piola, A. R., Garzoli, S. L., et al. (2013). Temporal variability of the meridional overturning circulation at 34.5°S: Results from two pilot boundary arrays in the South Atlantic. *Journal of Geophysical Research: Oceans*, *118*(12), 6461–6478. https://doi.org/10.1002/2013JC009228

Moat, B. I., Smeed, D. A., Frajka-Williams, E., Desbruyères, D. G., Beaulieu, C., Johns, W. E., et al. (2020). Pending recovery in the strength of the meridional overturning circulation at 26° N. *Ocean Science*, *16*(4), 863–874. https://doi.org/10.5194/os-16-863-2020

Petit, T., Lozier, M. S., Josey, S. A., & Cunningham, S. A. (2020). Atlantic deep water formation occurs primarily in the Iceland Basin and Irminger Sea by local buoyancy forcing. *Geophysical Research Letters*, *47*(22), 1–9. https://doi.org/10.1029/2020GL091028

Rahmstorf, S. (1996). On the freshwater forcing and transport of the Atlantic thermohaline circulation. *Climate Dynamics*, *12*, 799–811. https://doi.org/10.1007/s003820050144

Rahmstorf, S., Box, J. E., Feulner, G., Mann, M. E., Robinson, A., Rutherford, S., & Schaffernicht, E. J. (2015). Exceptional twentieth-century slowdown in Atlantic Ocean overturning circulation. *Nature Climate Change*, *5*(5), 475–480. https://doi.org/10.1038/nclimate2554

Roberts, C. D., Jackson, L., & McNeall, D. (2014). Is the 2004-2012 reduction of the Atlantic meridional overturning circulation significant? *Geophysical Research Letters*, *41*(9), 3204–3210. https://doi.org/10.1002/2014GL059473

Saunders, P. M., & King, B. A. (1995). Oceanic fluxes on the WOCE A11 section. *Journal of Physical Oceanography*, *25*, 1942–1958. https://doi.org/10.1175/1520-0485(1995)025<1942:ofotwa>2.0.co;2

Sévellec, F., & Sinha, B. (2018). Predictability of decadal Atlantic meridional overturning circulation variations. *Oxford Encyclopedia of Climate Science*. https://doi.org/10.1093/acrefore/9780190228620.013.81.hal-02136510

Sloyan, B. M., & Rintoul, S. R. (2001). The Southern Ocean limb of the global deep overturning circulation. *Journal of Physical Oceanography*, *31*(1), 143–173. https://doi.org/10.1175/1520-0485(2001)031<0143:tsolot>2.0.co;2

Srokosz, M., Baringer, M., Bryden, H., Cunningham, S., Delworth, T., Lozier, S., et al. (2012). Past, present, and future changes in the Atlantic meridional overturning circulation. *Bulletin of the American Meteorological Society*, *93*(11), 1663–1676. https://doi.org/10.1175/BAMS-D-11-00151.1

Srokosz, M. A., & Bryden, H. L. (2015). Observing the Atlantic meridional overturning circulation yields a decade of inevitable surprises. *Science*, *348*(6241). https://doi.org/10.1126/science.1255575

Talley, L. D. (2008). Freshwater transport estimates and the global overturning circulation: Shallow, deep and throughflow components. *Progress in Oceanography*, *78*(4), 257–303. https://doi.org/10.1016/j.pocean.2008.05.001

Talley, L. D., Feely, R. A., Sloyan, B. M., Wanninkhof, R., Baringer, M. O., Bullister, J. L., et al. (2016). Changes in ocean heat, carbon content, and ventilation: A review of the first decade of GO-SHIP global repeat hydrography. *Annual Review of Marine Science*, *8*(1), 185–215. https://doi.org/10.1146/annurev-marine-052915-100829

Thornalley, D. J. R., Oppo, D. W., Ortega, P., Robson, J. I., Brierley, C. M., Davis, R. E., et al. (2018). Anomalously weak Labrador Sea convection and Atlantic overturning during the past 150 years. *Nature*, *556*(7700), 227–230. https://doi.org/10.1038/s41586-018-0007-4

Weber, S. L., & Drijfhout, S. S. (2007). Stability of the Atlantic meridional overturning circulation in the last glacial maximum climate. *Geophysical Research Letters*, *34*(22), L22706. https://doi.org/10.1029/2007GL031437

Wefer, G., Berger, W. H., Siedler, G., & Webb, D. J. (1996). In G. Wefer, W. H. Berger, G. Siedler, & D. J. Webb (Eds.), *The South Atlantic: Present and past circulation*. Springer.

Weijer, W., Cheng, W., Drijfhout, S. S., Fedorov, A. V., Hu, A., Jackson, L. C., et al. (2019). Stability of the Atlantic meridional overturning circulation: A review and synthesis. *Journal of Geophysical Research: Oceans*, *124*(8), 5336–5375. https://doi.org/10.1029/2019JC015083

Weijer, W., de Ruijter, W. P. M., Dijkstra, H. A., & van Leeuwen, P. J. (1999). Impact of interbasin exchange on the Atlantic overturning circulation. *Journal of Physical OceanographyCO*, *29*(9), 2266–2284. https://doi.org/10.1175/1520-0485(1999)029<2266:ioieot>2.0.co;2

Weijer, W., & van Sebille, E. (2014). Impact of Agulhas leakage on the Atlantic overturning circulation in the CCSM4. *Journal of Climate*, *27*(1), 101–110. https://doi.org/10.1175/JCLI-D-12-00714.1

Woodgate, R. A., & Aagaard, K. (2005). Revising the Bering Strait freshwater flux into the Arctic ocean. *Geophysical Research Letters*, *32*. https://doi.org/10.1029/2004GL021747

Worthington, E. L., Moat, B. I., Smeed, D. A., Mecking, J. V., Marsh, R., & McCarthy, G. D. (2021). A 30-year reconstruction of the Atlantic meridional overturning circulation shows no decline. *Ocean Science*, *17*(1), 285–299. https://doi.org/10.5194/os-17-285-2021

Wunsch, C. (1978). The North Atlantic general circulation west of 50°W determined by inverse methods. *Reviews of Geophysics and Space Physics*, *16*(4), 583–620. https://doi.org/10.1029/rg016i004p00583

Wunsch, C. (1996). *The ocean circulation inverse problem*. Cambridge University Press.

References From the Supporting Information

Artana, C., Ferrari, R., Koenig, Z., Sennéchael, N., Saraceno, M., Piola, A. R., & Provost, C. (2018). Malvinas current volume transport at 41°S: A 24 yearlong time series consistent with mooring data from 3 decades and satellite altimetry. *Journal of Geophysical Research: Oceans*, *123*(1), 378–398. https://doi.org/10.1002/2017JC013600

Bersch, M., Yashayaev, I., & Koltermann, K. P. (2007). Recent changes of the thermohaline circulation in the subpolar North Atlantic. *Ocean Dynamics*, *57*(3), 223–235. https://doi.org/10.1007/s10236-007-0104-7

Curry, B., Lee, C. M., Petrie, B., Moritz, R. E., & Kwok, R. (2014). Multiyear volume, liquid freshwater, and sea ice transports through Davis Strait, 2004–10. *Journal of Physical Oceanography*, *44*(4), 1244–1266. https://doi.org/10.1175/jpo-d-13-0177.1

Ganachaud, A. S. (1999). *Large scale oceanic circulation and fluxes of freshwater, heat, nutrients and oxygen*. Massachusetts Institute of Technology and Woods Hole Oceanographic Institution. https://doi.org/10.1575/1912/4130

Ganachaud, A. S. (2003a). Error budget of inverse box models: The North Atlantic. *Journal of Atmospheric and Oceanic Technology*, *20*(11), 1641–1655. https://doi.org/10.1175/1520-0426(2003)020<1641:EBOIBM>2.0.CO;2

Hogg, N., Biscaye, P., Gardner, W., & Schmitz, W. J. (1982). On the transport and modification of Antarctic bottom water in the Vema channel. *Journal of Marine Research*, *40*, 231–263.

Hogg, N. G., & Owens, W. B. (1999). Direct measurement of the deep circulation within the Brazil Basin. *Deep Sea Research Part II: Topical Studies in Oceanography*, *46*(1–2), 335–353. https://doi.org/10.1016/S0967-0645(98)00097-6

Holliday, N. P., Bacon, S., Cunningham, S. A., Gary, S. F., Karstensen, J., King, B. A., et al. (2018). Subpolar North Atlantic overturning and gyre-scale circulation in the summers of 2014 and 2016. *Journal of Geophysical Research: Oceans*, *123*(7), 4538–4559. https://doi.org/10.1029/2018JC013841

Katsumata, K., & Fukasawa, M. (2011). Changes in meridional fluxes and water properties in the Southern Hemisphere subtropical oceans between 1992/1995 and 2003/2004. *Progress in Oceanography*, *89*(1–4), 61–91. https://doi.org/10.1016/j.pocean.2010.12.008

King, B. A., Sanchez-Franks, A., & Firing, Y. L. (2019). *RRS james cook cruise JC159 28 February - 11 April 2018. Hydrographic sections from the Brazil to the Benguela current across 24S in the Atlantic*, 60, (pp. 193). National Oceanography Centre Cruise Report.

Lazier, J., Hendry, R., Clarke, A., Yashayaev, I., & Rhines, P. (2002). Convection and restratification in the Labrador Sea, 1990–2000. *Deep Sea Research Part I: Oceanographic Research Papers*, *49*(10), 1819–1835. https://doi.org/10.1016/S0967-0637(02)00064-X

Lozier, M. S., Li, F., Bacon, S., Bahr, F., Bower, A. S., Cunningham, S. A., et al. (2019). *Meridional overturning circulation and the associated heat and freshwater transports observed by the OSNAP (Overturning in the Subpolar North Atlantic Program) array from 2014 to 2016*. Duke Digital Repository. https://doi.org/10.7924/r4z60gf0f

McDonagh, E. L., Bryden, H. L., King, B. A., & Sanders, R. J. (2008). The circulation of the Indian Ocean at 32°S. *Progress in Oceanography*, *79*(1), 20–36. https://doi.org/10.1016/j.pocean.2008.07.001

McDonagh, E. L., McLeod, P., King, B. A., Bryden, H. L., & Torres Valdés, S. (2010). Circulation, heat, and freshwater transport at 36°N in the Atlantic. *Journal of Physical Oceanography*, *40*(12), 2661–2678. https://doi.org/10.1175/2010JPO4176.1

Moat, B. I., Josey, S. A., Sinha, B., Blaker, A. T., Smeed, D. A., McCarthy, G. D., et al. (2016). Major variations in subtropical North Atlantic heat transport at short (5 day) timescales and their causes. *Journal of Geophysical Research: Oceans*, *121*(5), 3237–3249. https://doi.org/10.1002/2016JC011660

Morris, M. Y., Hall, M. M., St Laurent, L. C., & Hogg, N. G. (2001). Abyssal mixing in the Brazil basin. *Journal of Physical Oceanography*, *31*(11), 3331–3348. https://doi.org/10.1175/1520-0485(2001)031<3331:AMITBB>2.0.CO;2

Munk, W. H. (1966). Abyssal recipes. *Deep-Sea Research*, *13*, 707–730. https://doi.org/10.1016/0011-7471(66)90602-4

Parrilla, G., Lavín, A., Bryden, H. L., García, M., & Millard, R. (1994). Rising temperatures in the subtropical North Atlantic Ocean over the past 35 years. *Nature*, *369*(6475), 48–51. https://doi.org/10.1038/369048a0

Rhein, M., Mertens, C., & Roessler, A. (2019). Observed transport decline at 47°N, western Atlantic. *Journal of Geophysical Research: Oceans*, *124*, 4875–4890. https://doi.org/10.1029/2019jc014993

Robbins, P. E., & Toole, J. M. (1997). The dissolved silica budget as a constraint on the meridional overturning circulation of the Indian Ocean. *Deep Sea Research Part I: Oceanographic Research Papers*, *44*(5), 879–906. https://doi.org/10.1016/S0967-0637(96)00126-4

Siedler, G., Müller, T. J., Onken, R., Arhan, M., Mercier, H., King, B. A., & Saunders, P. M. (1996). The zonal WOCE sections in the south Atlantic. In G. Wefer, W. H. Berger, G. Siedler, & D. J. Webb (Eds.), *The South Atlantic: Present and past circulation* (pp. 83–104). Springer-Verlag. https://doi.org/10.1007/978-3-642-80353-6_5

Speer, K. G., Holfort, J., Reynaud, T., & Siedler, G. (1996). South Atlantic heat transport at 11°S. In *The South Atlantic: Present and past circulation* (pp. 105–120). https://doi.org/10.1007/978-3-642-80353-6_6

Toole, J. M., Curry, R., Joyce, T. M., McCartney, M., & Peña-Molino, B. (2011). Transport of the north Atlantic deep western boundary current about 39°N, 70°W: 2004-2008. *Deep-Sea Research Part II*, *58*, 1768–1780. https://doi.org/10.1016/j.dsr2.2010.10.058

Våge, K., Pickart, R. S., Spall, M. A., Valdimarsson, H., Jónsson, S., Torres, D. J., et al. (2011). Significant role of the North Icelandic Jet in the formation of Denmark Strait overflow water. *Nature Geoscience*, *4*, 723–727. https://doi.org/10.1038/ngeo1234

Warren, B. A., & Speer, K. G. (1991). Deep circulation in the eastern south Atlantic Ocean. *Deep Sea Research Part A. Oceanographic Research Papers*, *38*, S281–S322. https://doi.org/10.1016/s0198-0149(12)80014-8

Woodgate, R. A. (2018). Increases in the Pacific inflow to the Arctic from 1990 to 2015, and insights into seasonal trends and driving mechanisms from year-round Bering Strait mooring data. *Progress in Oceanography*, *160*, 124–154. https://doi.org/10.1016/j.pocean.2017.12.007

Woodgate, R. A., Aagaard, K., & Weingartner, T. J. (2005). Monthly temperature, salinity, and transport variability of the Bering Strait through flow. *Geophysical Research Letters*, *32*(4). https://doi.org/10.1029/2004GL021880

Yashayaev, I., & Loder, J. W. (2016). Recurrent replenishment of Labrador Sea Water and associated decadal-scale variability. *Journal of Geophysical Research: Oceans*, *121*(11), 8095–8114. https://doi.org/10.1002/2016JC012046

Yashayaev, I., & Loder, J. W. (2017). Further intensification of deep convection in the Labrador Sea in 2016. *Geophysical Research Letters*, *44*, 1429–1438. https://doi.org/10.1002/2016GL071668

Geophysical Research Letters

Supporting Information for

Thirty years of GOSHIP and WOCE data: Atlantic Overturning of mass, heat and freshwater transport

V. Caínzos[1], A. Hernández-Guerra[1], G. D. McCarthy[2], E. L. McDonagh[3,4], M. Cubas Armas[1], and M. D. Pérez-Hernández[1]

[1] Unidad Océano y Clima, Instituto de Oceanografía y Cambio Global, IOCAG, Universidad de Las Palmas de Gran Canaria, ULPGC, Unidad Asociada ULPGC-CSIC, Canary Islands, Spain.
[2] ICARUS, Department of Geography, Maynooth University, Maynooth, Ireland.
[3] NORCE Norwegian Research Centre, Bjerknes Centre for Climate Research, Bergen, Norway.
[4] National Oceanography Centre (NOC), Southampton SO14 3ZH, UK.

Contents of this file

Introduction

We have included a more detailed description of the inverse model, including the constraints, a priori uncertainties and weaknesses. There are also sensitivity tests confirming the robustness of the method used. Vertical section plots of potential temperature and salinity are presented for all sections used in each decade.

Text S1. Inverse box model configuration

CONSERVATION EQUATIONS

The inverse model for each decade links boxes between contiguous sections, from South to North. For each single box, the matrix form of the inverse model equation has the following form:

$$\begin{pmatrix} e_{A_{t,1}} & \cdots & e_{A_{t,n}} & e_{B_{t,1}} & \cdots & e_{B_{t,m}} & 1 & 1 \\ e_{A_{reg}} & \cdots & e_{A_{reg}} & 0 & \cdots & 0 & 0 & 0 \\ 0 & \cdots & 0 & e_{B_{reg}} & \cdots & e_{B_{reg}} & 0 & 0 \\ e_{A_{1,1}} & \cdots & e_{A_{1,n}} & e_{B_{1,1}} & \cdots & e_{B_{1,n}} & 1 & 1 \\ e_{A_{2,1}} & \cdots & e_{A_{2,n}} & e_{B_{2,1}} & \cdots & e_{B_{2,n}} & 0 & 0 \\ \vdots & \ddots & \vdots & \vdots & \ddots & \vdots & 0 & 0 \\ \vdots & \ddots & \vdots & \vdots & \ddots & \vdots & \vdots & \vdots \\ e_{A_{q-1,1}} & \cdots & e_{A_{q-1,n}} & e_{B_{q-1,1}} & \cdots & e_{B_{q-1,n}} & 0 & 0 \\ e_{A_{q,1}} & \cdots & e_{A_{q,n}} & e_{B_{q,1}} & \cdots & e_{B_{q,n}} & 0 & 0 \\ s_{A_{t,1}} & \cdots & s_{A_{t,n}} & 0 & \cdots & 0 & \overline{\left(\frac{s_{A_1}}{e_{A_1}}\right)} & 0 \\ 0 & \cdots & 0 & S_{B_{t,1}} & \cdots & S_{B_{t,m}} & 0 & \overline{\left(\frac{s_{B_1}}{e_{B_1}}\right)} \end{pmatrix} \begin{pmatrix} b_{A_1} \\ \vdots \\ b_{A_n} \\ b_{B_1} \\ \vdots \\ b_{B_m} \\ \Delta T_{A_{Ek}} \\ \Delta T_{B_{Ek}} \end{pmatrix} = \begin{pmatrix} y_{A_t} + y_{B_t} + T_{A_{Ek}} + T_{B_{Ek}} \\ y_{A_{reg}} \\ y_{B_{reg}} \\ y_{A_1} + y_{B_1} + T_{A_{Ek}} + T_{B_{Ek}} \\ y_{A_2} + y_{B_2} \\ \vdots \\ \vdots \\ y_{A_{q-1}} + y_{B_{q-1}} \\ y_{A_q} + y_{B_q} \\ z_t + T_{A_{Ek}} \cdot \overline{\left(\frac{s_{A_1}}{e_{A_1}}\right)} \\ z_{B_t} + T_{B_{Ek}} \cdot \overline{\left(\frac{s_{B_1}}{e_{B_1}}\right)} \end{pmatrix},$$

where n is the number of station pairs for section A, m is the number of station pairs for section B, q is the number of layers, b are the reference velocities for each station pair, ΔT_{Ek} is the Ekman transport correction, e is mass, s is salt, y is mass transport and z is the salt transport.

The first equation included in each box is the total conservation for the whole box (denoted with a t for total). This equation applies to all station pairs of A and B and consider both Ekman corrections, as the first layers must be corrected. The following equations are the regional constraints applied to section A, with different station pairs and neutral density layers affected. Similarly, regional equations for section B are found in subsequent files. The following 11 (q layers) equations correspond to the conservation of each layer between both sections with Ekman correction in the outcropping layers.

In addition to mass conservation, we have also constrained the salinity content of each single section A and B (last two equations). Using salinity instead of mass allows for changes in freshwater across the section while still conserving mass. The salinity transport constrained is 26.0 Sv, resulting from a Bering Strait mass transport of 0.8 Sv with an average salinity of 32.5. For mass conservation, the Ekman parameter used was 1. For salinity conservation, this parameter is expressed as the average ratio between salt and mass at the outcropping layer.

No other properties are conserved in these models. Heat and salt are largely dependent on mass and do not increase the rank of the matrix, therefore failing to add information to the system. The use of property anomalies increases the noise in the system solutions and does not provide a better solution to the inverse model. Top-to-bottom silica conservation has been applied in inverse models when the solution presented large imbalances on the silica budget as in the Indian Ocean (Robbins & Toole, 1997). In the Atlantic Ocean, and specifically in these inverse models, the models already provide

solution that satisfy the conservation of silica within each box. Therefore, we do not include these extra equations in the matrix as it would not increase the rank of the matrix or reduce the size of the uncertainties.

The 1990-99 inverse model has 643 unknowns in 105 equations, the 2000-09 model has 545 unknowns in 78 equations, and the 2010-19 inverse model has 589 unknowns and 77 equations. Therefore, the solutions come from a highly undetermined system of equations. The system unknowns include the velocities at the reference level and the adjustment to the Ekman transport in the first layer. The Gauss-Markov estimator is applied to solve these matrices (Wunsch, 1996).

REFERENCE LEVEL AND VELOCITIES

The choice of reference level is summarized in **Table S1**. In the South Atlantic, the general choice for reference level is the interphase between the southward flowing North Atlantic Deep Waters (NADW) and the northward flowing Antarctic Bottom Waters (AABW), which lies in the neutral density surface of 28.15 kg m^{-3} (Hernández-Guerra et al., 2019; McDonagh & King, 2005). Section A08 (11°S) in the decade of 1990-99 has basin-specific reference levels between 27.58 and 28.10 kg m^{-3} (Speer et al., 1996). In the North Atlantic subtropical gyre, the reference level of section A05 (24°N) is situated in the interphase between NADW and AABW, at 28.15 kg m^{-3} for the 1990-99 and 2000-09 decades and at 28.04 kg m^{-3} for the last decade (Fu et al., 2018; Hernández-Guerra et al., 2014). Section A02 (47°N) for the 1990-99 decade presents a reference level at 28.15 kg m^{-3} at the interphase between NADW and AABW, whereas for the decade of 2010-19 it is at the interphase between the MOC upper and lower limb at 27.84 kg m^{-3} (Ganachaud, 1999). At A03 (36°N), the reference level at the interphase between NADW and AABW is at a neutral density of 28.04 kg m^{-3} (McDonagh et al., 2010). The northernmost sections at 55°N (AR07W+AR07E) show better results when choosing the reference level at the interphase between the MOC upper and lower limb, which lies at 27.84 kg m^{-3} (Holliday et al., 2018; Lozier et al., 2019).

A PRIORI ESTIMATES AND UNCERTAINTIES

The Gauss-Markov method solves this system of equations with a minimum error variance solution from the initial estimates of the unknowns (the velocities at the reference level, b, and the corrections to the Ekman transport, ΔT_{Ek}) (Wunsch, 1996). To solve it, we first need a priori estimates and uncertainties that give an initial approximation to the actual value. The preliminary variance of the adjusted velocity at the reference level is 8 cm^2 s^{-2} for the station pairs closer to coast, where shear is stronger and 4 cm^2 s^{-2} in the deepest stations. The initial estimates for the mass transport are 9 Sv^2 for the net mass transport between two sections, therefore allowing for compensation within each box. For layer conservation, the variance is between 13 and 1 Sv^2, decreasing towards deeper layers. The salinity uncertainties are computed as the square of the uncertainty of the Bering Strait transport (0.6 Sv) times the square of the ration between the total salt transport and the mass transport of each section.

Despite obtaining similar results, this study provides smaller uncertainties than other global inverse solutions (Ganachaud, 2003b) and decadal studies (Fu et al., 2020). This was achieved by using a simpler model with only the velocities at the reference level and the Ekman adjustments as unknowns.

Some of the weaknesses of the inverse model are related to the accurate calculation of the geostrophic transport before the inverse model. We have assumed linear bottom topography between the deepest common level of each station to compute the transport of each bottom triangle. There are uncertainties associated to this approximation, in the order of 1 Sv, but can increase in areas of boundary currents along sloping topography (Ganachaud, 2003a; Elaine L. McDonagh et al., 2008; Robbins & Toole, 1997).

The Ekman transport can also be an issue when adjusting the geostrophic transport in surface layers. We believe that the geostrophic calculation of each section is balanced by the Ekman transport for the time of the cruise. There is an adjustment for the instantaneous response of this wind forcing on the upper layers. Using the Ekman transport of the time of the cruise we remove the effect of the seasonal or monthly variability in upper layers. In any case, the Ekman transport is adjusted in the inverse model.

DIANEUTRAL ESTIMATES

Dianeutral transport (both advection velocity (ω) and diffusion coefficient (κ_z)) were calculated in every box delimited by two sections and two neutral density surfaces. The small imbalance between horizontal mass transport within each box after the inverse model was compensated by an adjustment with a vertical transport and its associated ω across neutral density surfaces. The remaining changes in vertical heat transport are explained by diffusion processes (Hernández-Guerra & Talley, 2016; Hogg et al., 1982; Morris et al., 2001; Munk, 1966). Dianeutral diffusion coefficient κ_z is not shown in this paper.

Text S2. Sensitivity tests

Several sensitivity tests were conducted to determine the best configuration of the inverse models. The tightness of the constraints on regional and topographic features of the Southern Hemisphere were assessed by removing the constraints on section A10 (30°S). The results for each constraint are in **Table S6**. The boundary currents display some differences, but it has not been transmitted to the net heat and freshwater budget, which remain the same, and has not altered the values of the freshwater overturning.

We have also conducted sensibility tests to understand the importance of the temporal variability of the Bering Strait salinity and transport (**Table S7**). We have changed the average salinity of the Bering Strait from 31.5 to 33.5 (Woodgate et al., 2005) and the Bering Strait transport for the last two decades from -0.8 ± 0.6 to -1.0 ± 0.5 Sv (Woodgate, 2018). These changes affect basically the throughflow components, but the overturning and horizontal components are not changed.

Text S3. Heat and freshwater comparison with RAPID and OSNAP time series

The RAPID-MOCHA mean heat transports of 1.3 ± 0.4 PW and 1.2 ± 0.4 PW for the decades of 2000-09 and 2010-19, respectively (Moat et al., 2016) are not significantly different than the values of the inverse model (0.97 ± 0.09 and 1.13 ± 0.07 PW, respectively) for the section 24°N. In the SPNA, the mean heat transport product estimated from OSNAP (Lozier et al., 2019; Lozier et al., 2019) for the Eastern subbasin at 55°N (0.38 ± 0.02 PW) is similar to the inverse model value (0.29 ± 0.06 PW). The values for the Western subbasin at 55°N are very small in both cases (0.01 ± 0.02 PW for the inverse model and 0.08 ± 0.004 PW for OSNAP), and the values for the whole basin are comparable (0.30 ± 0.05 PW for the inverse model and 0.46 ± 0.02 PW for OSNAP), although different, partly because OSNAP data are not available for the whole decade. These results confirm the importance of the Eastern basin (55°N East) in the export of heat from the Atlantic to the Arctic Ocean, carried by the NAC in the upper layers.

The mean freshwater divergence transport across the whole OSNAP section (-0.32 ± 0.01 Sv) (Lozier et al. 2019; Lozier et al., 2019) in the 2010-19 decade is stronger than in the inverse model (-0.11 ± 0.11 Sv). In the inverse model, there is a southward freshwater transport (-0.17 ± 0.09 Sv) in the Eastern subbasin, that is basically unaltered by the no significant northward transport in the Western subbasin (0.06 ± 0.10 Sv). OSNAP data suggest, in turn, that both subbasins contribute similarly to the southward freshwater transport across the whole section (-0.18 ± 0.01 Sv and -0.14 ± 0.01 Sv for the West and East subbasins, respectively).

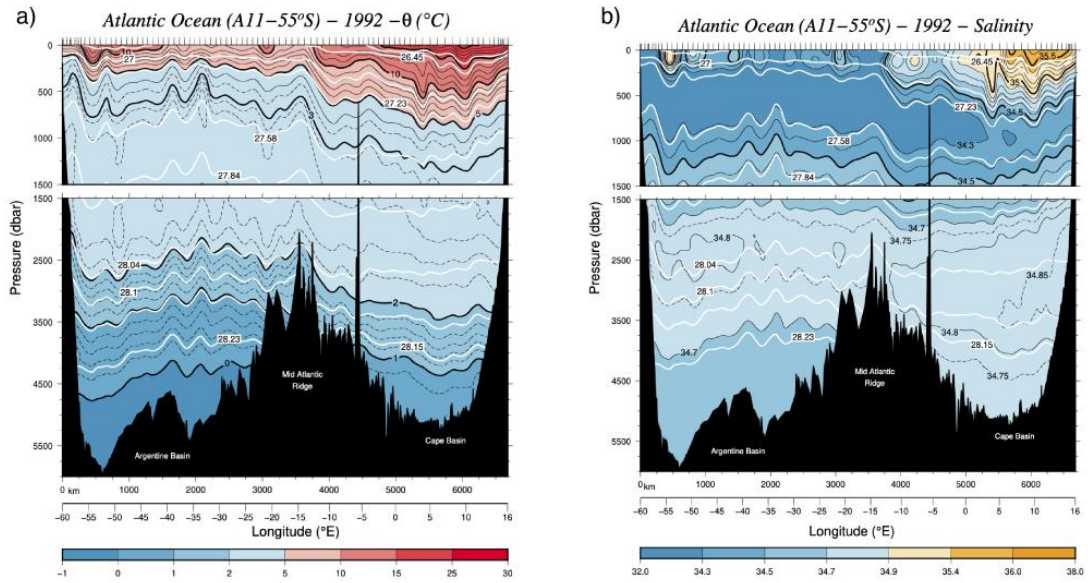

Figure S1. Vertical sections of potential temperature and salinity for each hydrographic section used in the inverse models. Black lines represent the values of potential temperature or salinity, and white lines are the interphases of neutral density that divide each layer of the inverse model.

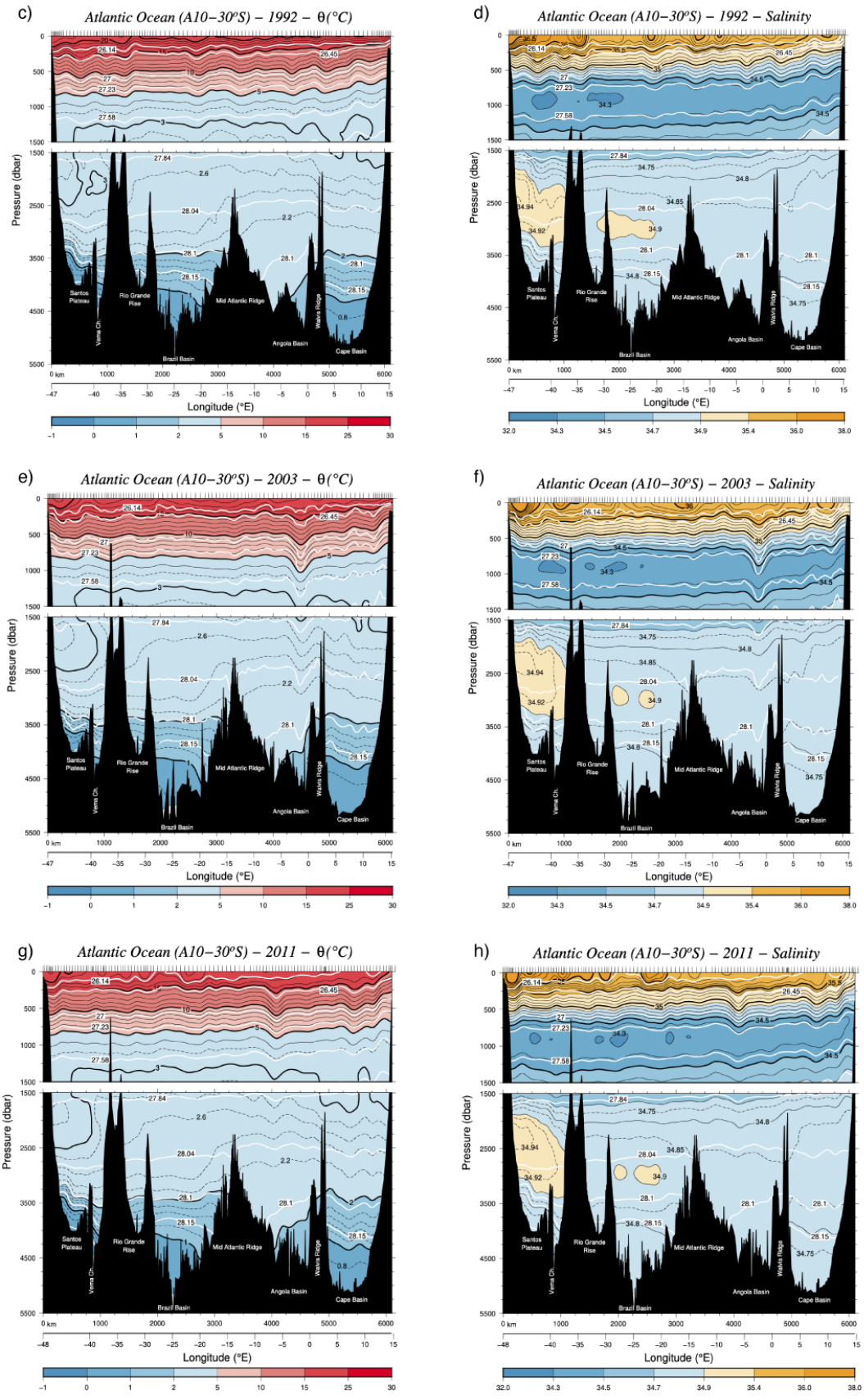
c)
Atlantic Ocean (A10–30°S) – 1992 – θ(°C)
d)
Atlantic Ocean (A10–30°S) – 1992 – Salinity
e)
Atlantic Ocean (A10–30°S) – 2003 – θ(°C)
f)
Atlantic Ocean (A10–30°S) – 2003 – Salinity
g)
Atlantic Ocean (A10–30°S) – 2011 – θ(°C)
h)
Atlantic Ocean (A10–30°S) – 2011 – Salinity
Pressure (dbar)
Longitude (°E)
Santos Plateau
Rio Grande Rise
Vema Ch.
Mid Atlantic Ridge
Walvis Ridge
Brazil Basin
Angola Basin
Cape Basin

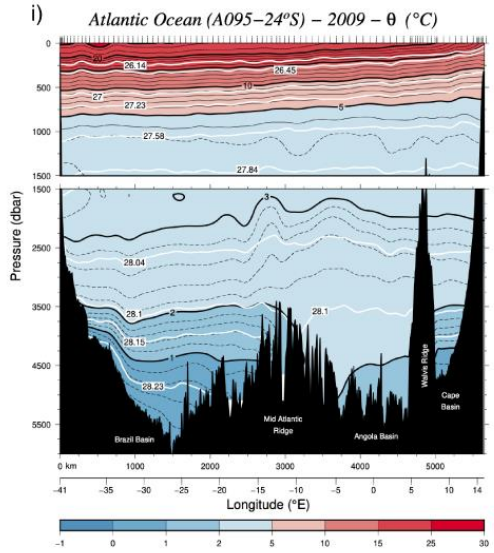
i)
Atlantic Ocean (A095–24°S) – 2009 – θ (°C)
Pressure (dbar)
Longitude (°E)
Brazil Basin
Mid Atlantic Ridge
Angola Basin
Walvis Ridge
Cape Basin

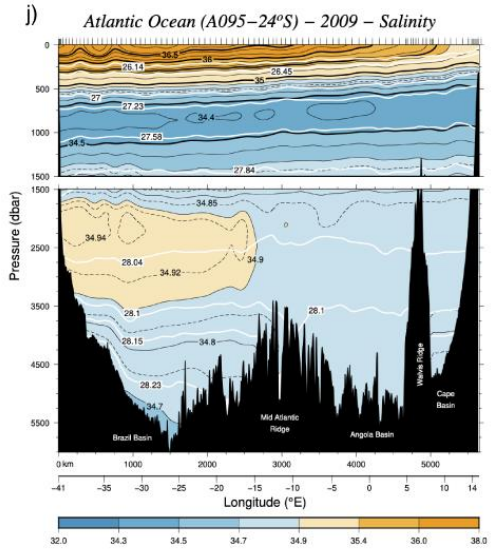
j)
Atlantic Ocean (A095–24°S) – 2009 – Salinity
Pressure (dbar)
Longitude (°E)
Brazil Basin
Mid Atlantic Ridge
Angola Basin
Walvis Ridge
Cape Basin

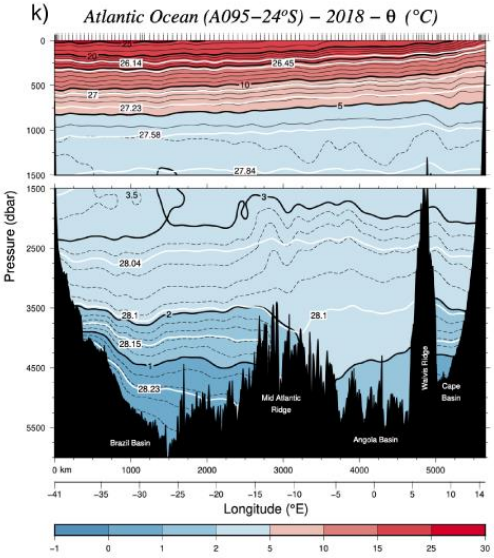
k)
Atlantic Ocean (A095–24°S) – 2018 – θ (°C)
Pressure (dbar)
Longitude (°E)
Brazil Basin
Mid Atlantic Ridge
Angola Basin
Walvis Ridge
Cape Basin

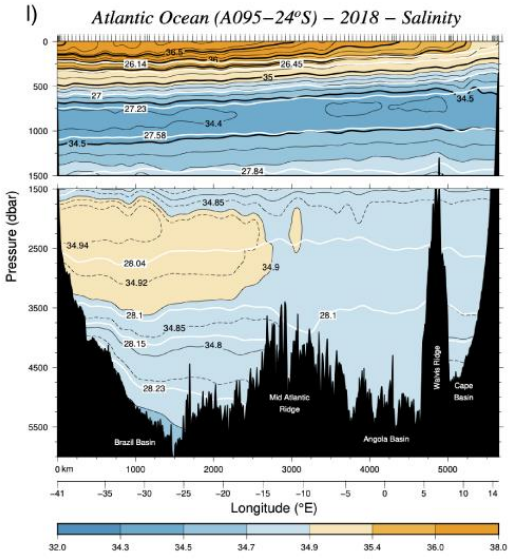
l)
Atlantic Ocean (A095–24°S) – 2018 – Salinity
Pressure (dbar)
Longitude (°E)
Brazil Basin
Mid Atlantic Ridge
Angola Basin
Walvis Ridge
Cape Basin

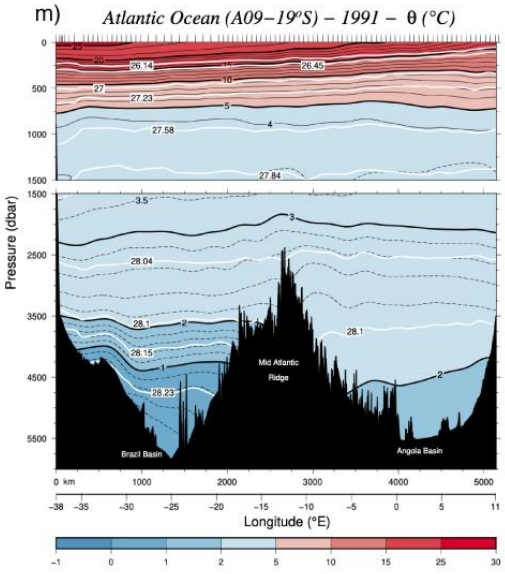
m)
Atlantic Ocean (A09–19°S) – 1991 – θ (°C)
Pressure (dbar)
Mid Atlantic Ridge
Brazil Basin
Angola Basin
Longitude (°E)

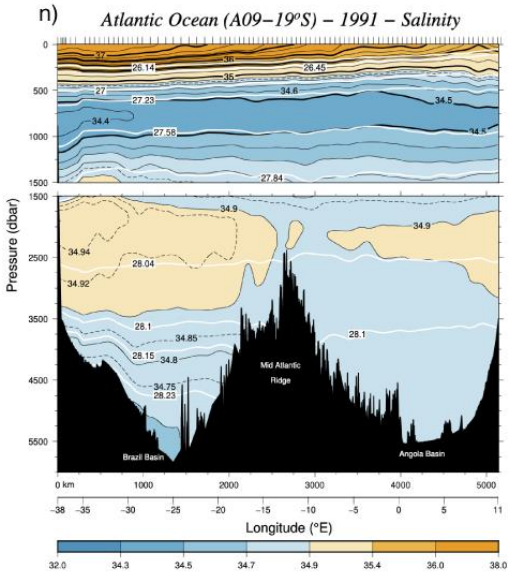
n)
Atlantic Ocean (A09–19°S) – 1991 – Salinity
Pressure (dbar)
Mid Atlantic Ridge
Brazil Basin
Angola Basin
Longitude (°E)

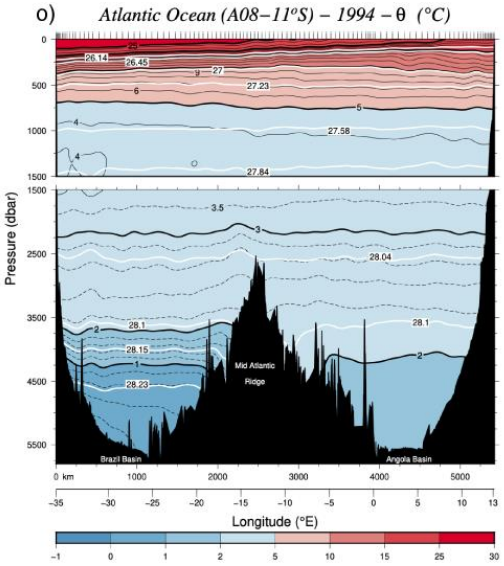
o) Atlantic Ocean (A08–11°S) – 1994 – θ (°C)
Pressure (dbar)
Mid Atlantic Ridge
Brazil Basin
Angola Basin
0 km
Longitude (°E)

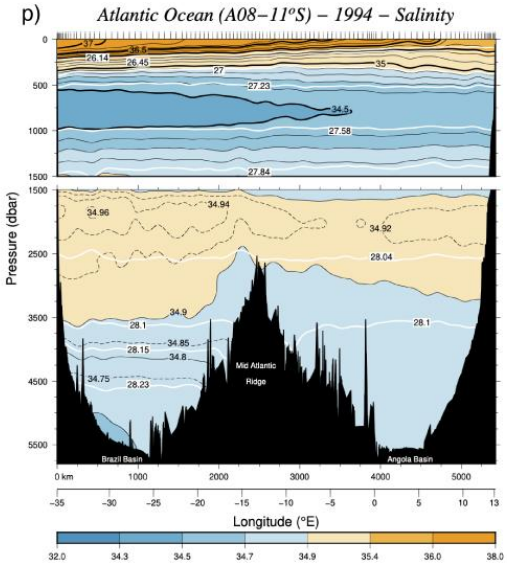
p) Atlantic Ocean (A08–11°S) – 1994 – Salinity
Pressure (dbar)
Mid Atlantic Ridge
Brazil Basin
Angola Basin
0 km
Longitude (°E)

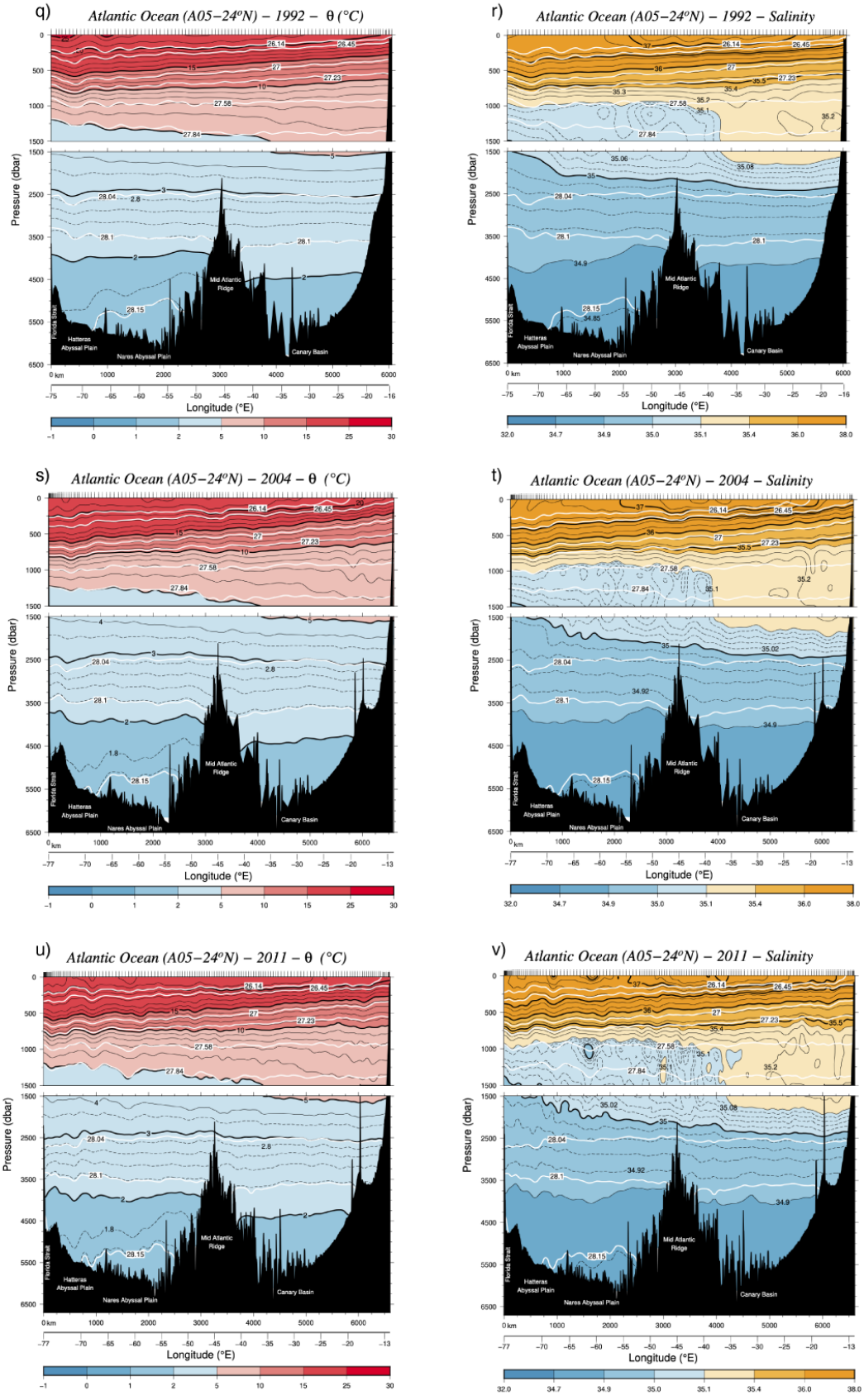
q) Atlantic Ocean (A05–24°N) – 1992 – θ (°C)
r) Atlantic Ocean (A05–24°N) – 1992 – Salinity
s) Atlantic Ocean (A05–24°N) – 2004 – θ (°C)
t) Atlantic Ocean (A05–24°N) – 2004 – Salinity
u) Atlantic Ocean (A05–24°N) – 2011 – θ (°C)
v) Atlantic Ocean (A05–24°N) – 2011 – Salinity
Pressure (dbar)
Longitude (°E)
Mid Atlantic Ridge
Florida Strait
Hatteras Abyssal Plain
Nares Abyssal Plain
Canary Basin

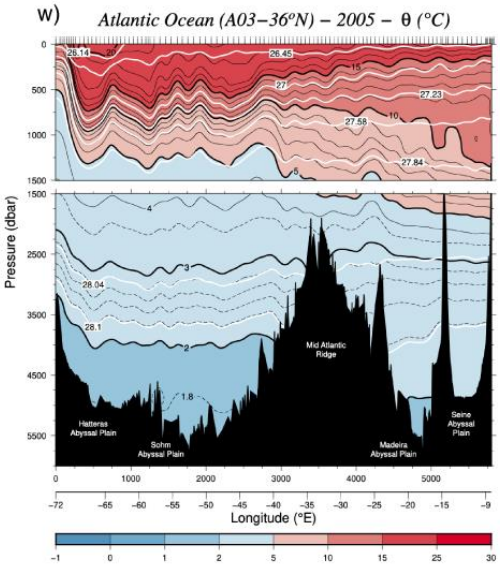
w)
Atlantic Ocean (A03−36ºN) − 2005 − θ (°C)
Pressure (dbar)
Longitude (°E)
Mid Atlantic Ridge
Hatteras Abyssal Plain
Sohm Abyssal Plain
Madeira Abyssal Plain
Seine Abyssal Plain

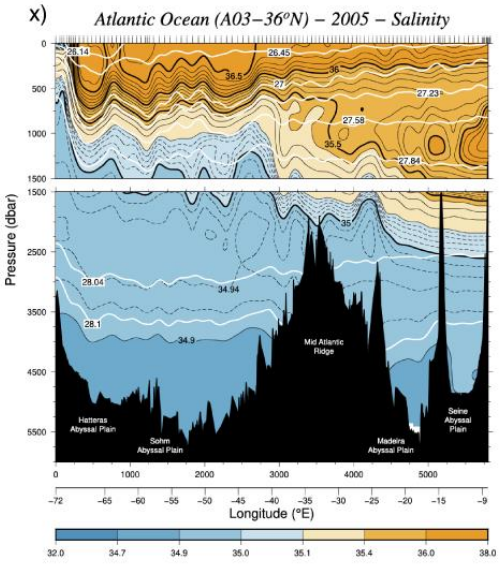
x)
Atlantic Ocean (A03−36ºN) − 2005 − Salinity
Pressure (dbar)
Longitude (°E)
Mid Atlantic Ridge
Hatteras Abyssal Plain
Sohm Abyssal Plain
Madeira Abyssal Plain
Seine Abyssal Plain

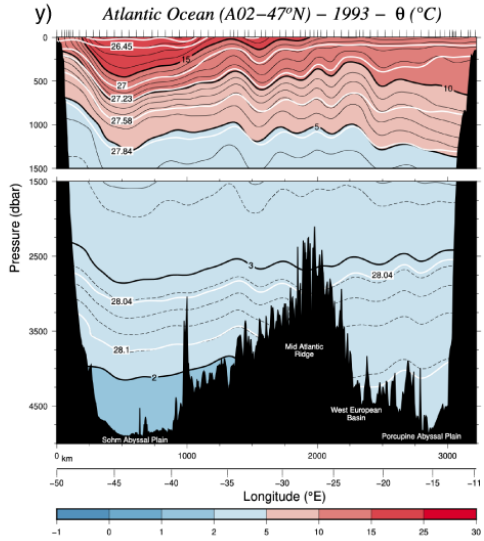
y) Atlantic Ocean (A02–47°N) – 1993 – θ (°C)
Pressure (dbar)
Mid Atlantic Ridge
West European Basin
Sohm Abyssal Plain
Porcupine Abyssal Plain
Longitude (°E)

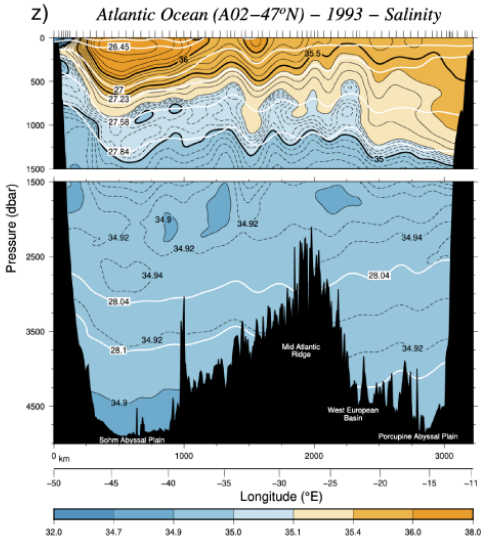
z) Atlantic Ocean (A02–47°N) – 1993 – Salinity
Pressure (dbar)
Mid Atlantic Ridge
West European Basin
Sohm Abyssal Plain
Porcupine Abyssal Plain
Longitude (°E)

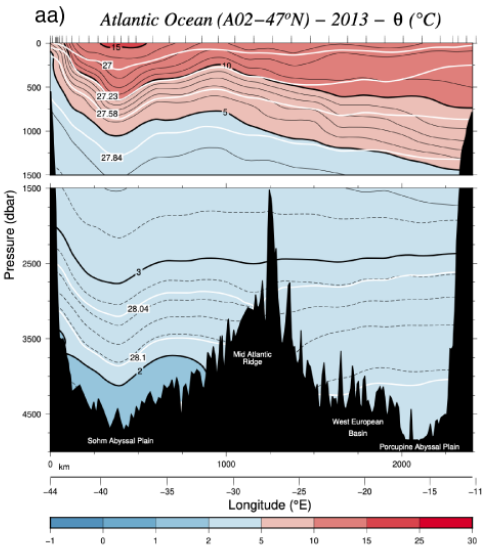
aa) Atlantic Ocean (A02–47°N) – 2013 – θ (°C)
Pressure (dbar)
Mid Atlantic Ridge
West European Basin
Sohm Abyssal Plain
Porcupine Abyssal Plain
Longitude (°E)

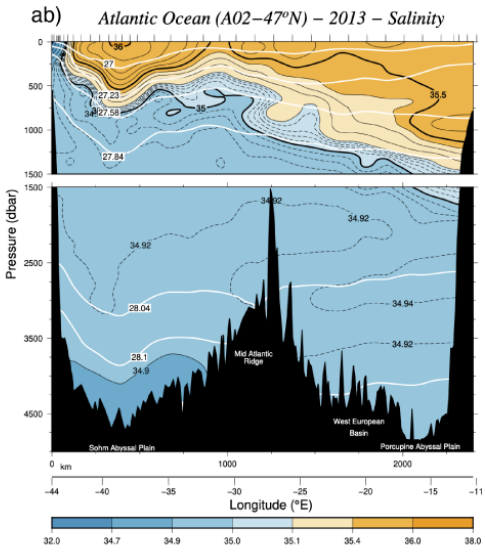
ab) Atlantic Ocean (A02–47°N) – 2013 – Salinity
Pressure (dbar)
Mid Atlantic Ridge
West European Basin
Sohm Abyssal Plain
Porcupine Abyssal Plain
Longitude (°E)

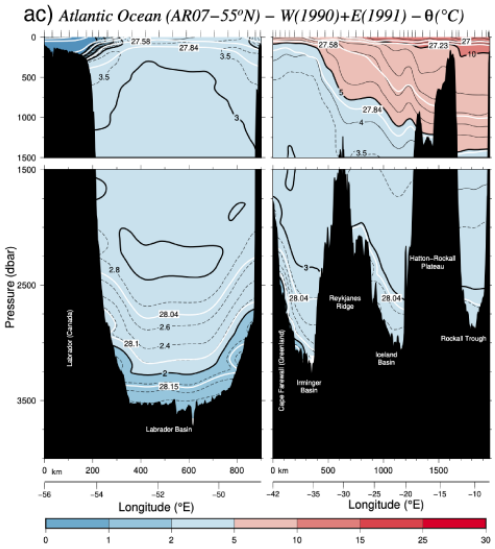
ac) Atlantic Ocean (AR07−55ºN) − W(1990)+E(1991) − θ(°C)
Pressure (dbar)
Longitude (°E)
Labrador (Canada)
Cape Farewell (Greenland)
Labrador Basin
Irminger Basin
Iceland Basin
Reykjanes Ridge
Hatton−Rockall Plateau
Rockall Trough

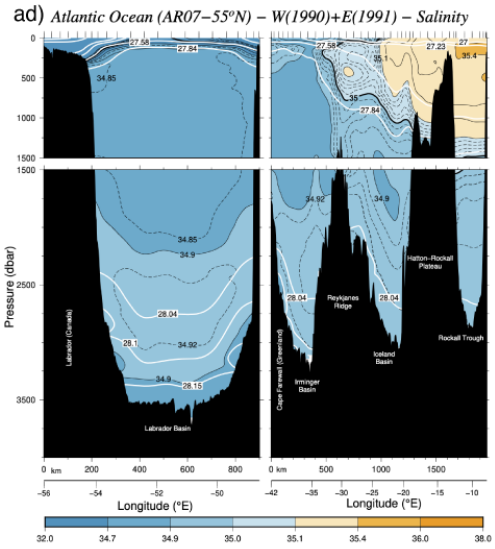
ad) Atlantic Ocean (AR07−55ºN) − W(1990)+E(1991) − Salinity
Pressure (dbar)
Longitude (°E)
Labrador (Canada)
Cape Farewell (Greenland)
Labrador Basin
Irminger Basin
Iceland Basin
Reykjanes Ridge
Hatton−Rockall Plateau
Rockall Trough

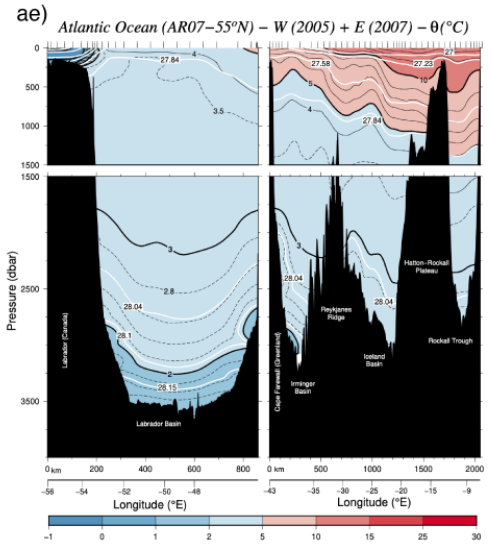
ae) Atlantic Ocean (AR07−55ºN) − W (2005) + E (2007) − θ(°C)
Pressure (dbar)
Longitude (°E)
Labrador (Canada)
Cape Farewell (Greenland)
Labrador Basin
Irminger Basin
Iceland Basin
Reykjanes Ridge
Hatton−Rockall Plateau
Rockall Trough

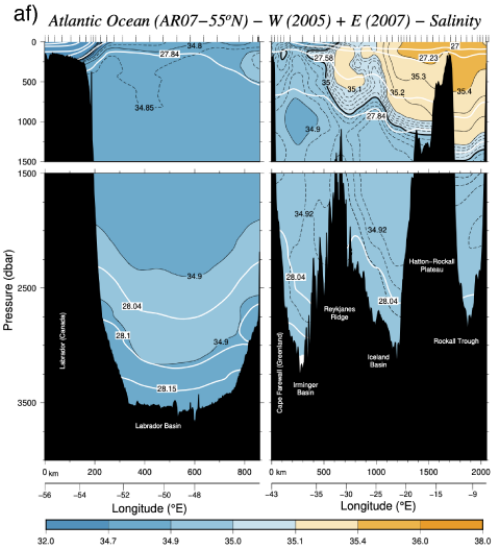
af) Atlantic Ocean (AR07−55ºN) − W (2005) + E (2007) − Salinity
Pressure (dbar)
Longitude (°E)
Labrador (Canada)
Cape Farewell (Greenland)
Labrador Basin
Irminger Basin
Iceland Basin
Reykjanes Ridge
Hatton−Rockall Plateau
Rockall Trough

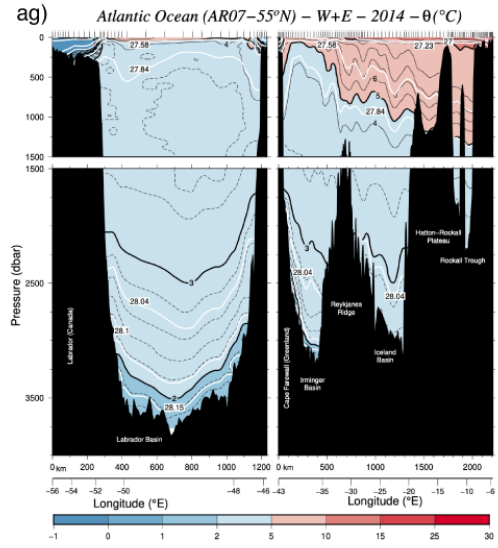
ag) Atlantic Ocean (AR07−55ºN) − W+E − 2014 − θ(°C)
Pressure (dbar)
Longitude (°E)
Labrador (Canada)
Cape Farewell (Greenland)
Labrador Basin
Irminger Basin
Iceland Basin
Reykjanes Ridge
Hatton−Rockall Plateau
Rockall Trough

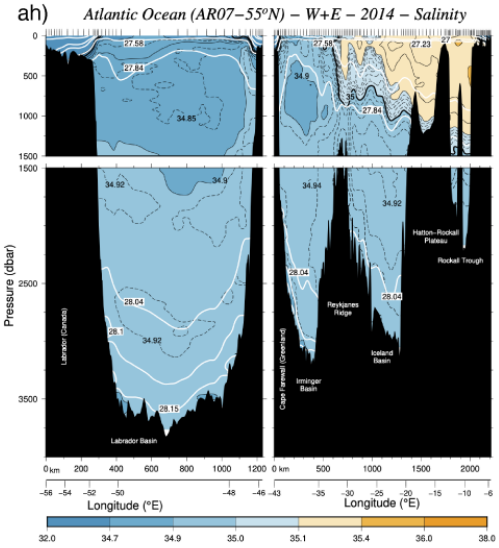
ah) Atlantic Ocean (AR07−55ºN) − W+E − 2014 − Salinity
Pressure (dbar)
Longitude (°E)
Labrador (Canada)
Cape Farewell (Greenland)
Labrador Basin
Irminger Basin
Iceland Basin
Reykjanes Ridge
Hatton−Rockall Plateau
Rockall Trough

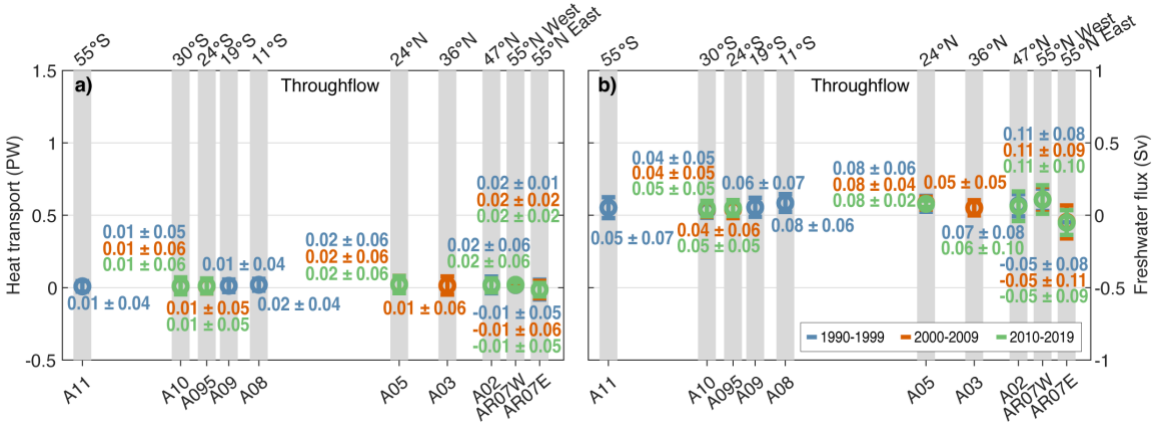

Figure S2. Heat (a) and freshwater (b) transport throughflow component for each latitude and decade. The gray bars mark the nominal latitude of each zonal section, and the colors represent each decade. The left panel is the heat transport in PW, and the panel on the right is the freshwater flux in Sv. The uncertainties associated with the heat and freshwater transports are part of the results of the inverse model solved using the Gauss-Markov estimator.

Table S1. Zonal sections used for each decade, including the reference layer where no-motion is assumed. The Ekman transport is computed for the time of the cruise using NCEP-NCAR products of wind stress.

Section	Year	Latitude	Country	PI	Reference	No. stns	Ref. layer	TEk (Sv)
A11	1992	30-45°S	UK	P. Saunders	(Saunders & King, 1995)	91	28.15	3.1 ± 0.4
A10	1992	30°S	DE	T. Müller	(Siedler et al., 1996)	110	28.15	-0.3 ± 0.2
A09	1991	19°S	DE	G. Siedler	(Siedler et al., 1996)	89	28.15	-4.7 ± 0.3
A08	1994	11°S	DE	T. Müller	(Siedler et al., 1996)	110	27.58-28.10	-8.3 ± 0.7
A05	1992	24.5°N	SP	G. Parrilla	(Parrilla et al., 1994)	11+99	28.15	5.8 ± 0.2
A02	1993	40-50°N	DE	A. Sy	(Koltermann et al., 1999)	74	28.15	-0.56 ± 0.15
AR07W	1990	55-60°N	CA	J. Lazier	(Lazier et al., 2002)	22	27.84	-0.02 ± 0.04
AR07E	1991	55-60°N	UK	J. Gould	(Våge et al., 2011)	38	27.84	-0.76 ± 0.11
A10	2003	30°S	JA	Y. Yoshikawa	(Katsumata & Fukasawa, 2011)	111	28.15	-0.5 ± 0.2
A095	2009	24°S	UK	B. King	(Johns et al., 2011)	94	28.15	-3.3 ± 0.1
A05	2004	24.5°N	UK	S. Cunningham	(Bryden et al., 2005)	9+115	28.15	3.9 ± 0.4
A03	2005	36°N	UK	E. McDonagh	(McDonagh et al., 2010)	112	28.04	-0.2 ± 0.2
AR07W	2005	55-60°N	CA	G. Harrison	(Bersch et al., 2007; Våge et al., 2011)	24	27.84	-0.01 ± 0.02
AR07E	2007	55-60°N	NE	G.-J. Brummer	(Yashayaev & Loder, 2016, 2017)	42	27.84	-1.51 ± 0.15
A10	2011	30°S	US	M. Baringer & A. Macdonald	(Hernández-Guerra et al., 2019)	120	28.15	-3.5 ± 0.4
A095	2018	19°S	UK	B. King	(King et al., 2019)	117	28.15	-1.8 ± 0.3
A05	2011	24.5°N	SP	A. Hernández-Guerra	(Hernández-Guerra et al., 2014)	14+152	28.04	3.9 ± 0.5
A02	2013	40-50°N	DE	D. Kieke	(Rhein et al., 2019)	39	27.84	-0.48 ± 0.13
AR07W	2014	55-60°N	UK	B. King & P. Holliday	(Lozier et al., 2019)	40	27.84	0.04 ± 0.05
AR07E	2014	55-60°N	UK	B. King & P. Holliday	(Lozier et al., 2019)	103	27.84	-0.30 ± 0.07

Table S2. Compilation of mass transport (Sv) values for other large scale box inverse models.

			A11	A10	A095	A09	A08	A05	A03	A02	AR07W+AR07E	AR07W	AR07E
Reference	Period	layers	55°S	30°S	24°S	19°S	11°S	24°N	36°N	47°N	55°N	53°N	58°N
This model (decade 1990-99)	1990-99	Upper	16.2 ± 1.9	17.6 ±1.0		19.8 ± 1.0	18.3 ± 0.9	17.7 ± 1.3		15.7 ± 1.8	12.0 ± 2.6	-0.9 ± 0.8	12.9 ± 2.5
		Deep	-20.8 ± 2.3	-21.7 ± 2.1		-21.9 ± 2.3	-20.7 ± 2.0	-18.8 ± 2.1		-16.6 ± 2.2	-12.8 ± 2.6	-0.7 ± 0.9	-12.1 ± 2.4
		Bottom	3.8 ± 1.7	3.5 ± 1.2		1.3 ± 0.9	1.2 ± 1.2	0.1 ± 0.9					
(Ganachaud, 2003)	1990-99	Upper	8 ± 3	18 ± 3		26 ± 3	28 ± 4	14 ± 2		19 ± 2			
		Deep	-18 ± 4	-23 ± 3		-23 ± 3	-23 ± 4	-18.5 ± 2		-16 ± 2			
		Bottom	5 ± 2	6 ± 1.3		3.4 ± 1.1	3.1 ± 1.5	1 ± 1		0			
(Lumpkin & Speer, 2007)	1990-99	MOC	12.4 ± 2.6				16.2 ± 3.0	18.0 ± 2.5		16.3 ± 2.7	17.0 ± 4.3*		
(Sloyan & Rintoul, 2001)	1988-89	Upper		9.7 ± 0.4 †		16.5± 0.6 ‡							
		Deep		-17.8 ± 2.1		-20.0 ± 2.4							
		Bottom		7.3 ± 1.7		5.2 ± 1.6							
(Macdonald, 1995)	1981-1990	Upper			6.5 ± 0.6 §	5.3 ± 0.9 ¶	9.9 ± 0.6	15.5 ± 0.9	10.5 ± 1.3	23.2 ± 0.8			
		Deep			-20.1 ± 1.2	-21.0 ± 3.1	-27.5 ± 1.4	-16.8 ± 1.2	-11.5 ± 1.6	-24.3 ± 1.3			
		Bottom			5.9 ± 0.9	3.1 ± 1.1	3.5 ± 1.0	0.4 ± 0.8					
(Fu et al., 2020)	1990-99	MOC						16.7 ± 2.4			15.4 ± 7.7	1.5 ± 3.3	15.8 ± 4.5
	2000-09	MOC						14.8 ± 2.2			15.6 ± 3.9	0.5 ± 0.9	16.6 ± 3.3
	2010-19	MOC						16.8 ± 3.1			13.4 ± 7.5	2.0 ± 3.5	14.9 ± 5.0

* only AR07E † SAVE4 ‡ SAVE2 § 23°S ¶ SAVE 3 leg3 + leg4 (17°S)

Table S3. Regional constraints applied to each section for the 1990-99 inverse model. The sixth column represents the imposed value in the model; the seventh column is the mass transport before the model, and the eighth column is the value after the inverse model. The uncertainties for the mass transport adjusted with the inverse model (eighth column) are part of the results of the inverse model using the Gauss-Markov estimator.

Salt constraints	Long	Depth	Stations	Layers	Constraint value (10^{-3} Sv psu)	Initial transport (10^{-3} Sv psu)	Adjusted transport (10^{-3} Sv psu)	References
A11 (1992) Bering Strait	All	All	1:90	1:11	-26 ± 21	360	-26 ± 8	(McDonagh et al., 2015)
A10 (1992) Bering Strait	All	All	1:110	1:11	-26 ± 21	864	-28 ± 6	(McDonagh et al., 2015)
A09 (1991) Bering Strait	All	All	1:93	1:11	-26 ± 21	1548	-20 ± 7	(McDonagh et al., 2015)
A08 (1994) Bering Strait	All	All	1:109	1:11	-26 ± 22	486	-19 ± 6	(McDonagh et al., 2015)
A05 + Florida (1992) Bering Strait	All	All	11:108	1:11	-26 ± 22	484	-26 ± 7	(McDonagh et al., 2015)
A02 (1993) Bering Strait	All	All	1:73	1:11	-26 ± 22	225	-24 ± 8	(McDonagh et al., 2015)
A07 = AR07W + AR07E Bering Strait (total)	All	All	1:58	1:11	-26 ± 21	238	-28 ± 9	(McDonagh et al., 2015)

Table S3 (cont)

Mass constraints	Long	Depth	Stations	Layers	Constraint value (Sv)	Initial transport (Sv)	Adjusted transport (Sv)	References
A11 (1992)								
WBC (Malvinas current)	60-57.8°W	All	1:4	1:11	37.1 ± 6.6	37.1	38.0 ± 2.0	(Artana et al., 2018)
Cape Basin AABW	8.2°W-10.9°E	Bottom	58:80	9:11	0 ± 0.5	1.0	0.0 ± 0.9	(McDonagh & King, 2005)
Argentine Basin AABW	57-15°W	Bottom	9:51	9:11	6 ± 1	-1.5	5.9 ± 1.6	(McDonagh & King, 2005)
A10 (1992)								
Brazil basin	45-15.3°W	Bottom	12:63	9:11	6.9 ± 1.8	3.0	4.5 ± 1.7	(Hogg & Owens, 1999)
Vema channel	39.7-37.7°W	AABW	21:25	9:11	4.0 ± 0.4	1.5	3.8 ± 0.4	(Hogg et al., 1982)
Walvis R. North	7.3°W-1.7°E	Bottom	75:87	9:11	0 ± 1	-0.2	-0.5 ± 0.9	(Warren & Speer, 1991)
Walvis R. South	2.2-13.4°E	Bottom	88:106	9:11	0 ± 1	0.7	-0.8 ± 1.3	(Warren & Speer, 1991)
Brazil current	Coast-44.8°W	Surf - interm	1:12	1:7	-38.9 ± 2.1	-16.3	-38.2 ± 1.3	(Hernández-Guerra et al., 2019)
Benguela current	11.8°E-Coast	Surf - interm	101:110	1:7	26.3 ± 2.4	19.7	25.8 ± 1.4	(Hernández-Guerra et al., 2019)
A05 + Florida (1992)								
Florida Current	All	All	1:10	1:5	31.8 ± 3.5	31.8	31.8 ± 0.3	Florida Current Project
AR07W (1990)								
Bering Strait (Davis Strait)	All	All	1:21	1:11	-1.6 ± 0.2	1.0	-1.6 ± 1.2	(Curry et al., 2014)
AR07E (1993)								
Bering Strait (East)	All	All	22:58	1:11	0.80 ± 0.63	5.7	0.7 ± 3.5	(Lozier et al., 2019)

Table S4. Regional constraints applied to each section for the 2000-09 inverse model. The sixth column represents the imposed value in the model; the seventh column is the mass transport before the model, and the eighth column is the value after the inverse model. The uncertainties for the mass transport adjusted with the inverse model (eighth column) are part of the results of the inverse model using the Gauss-Markov estimator.

Salt constraints	Long	Depth	Stations	Layers	Constraint value (10^{-3} Sv psu)	Initial transport (10^{-3} Sv psu)	Adjusted transport (10^{-3} Sv psu)	Reference
A10 (2003) Bering Strait	All	All	1:110	1:11	-26 ± 21	625	-28 ± 7	(McDonagh et al., 2015)
A095 (2009) Bering Strait	All	All	1:93	1:11	-26 ± 21	1376	-16 ± 8	(McDonagh et al., 2015)
A05 + Florida (2004) Bering Strait	All	All	1:122	1:11	-26 ± 21	676	-30 ± 8	(McDonagh et al., 2015)
A03 (2005) Bering Strait	All	All	1:122	1:11	-26 ± 21	1110	-19 ± 9	(McDonagh et al., 2015)
A07 = AR07W + AR07E Bering Strait (total)	All	All	1:66	1:11	-26 ± 20	-218	-29 ± 8	(McDonagh et al., 2015)

Table S4 (cont)

Mass constraints	Long	Depth	Stations	Layers	Constraint value (Sv)	Initial transport (Sv)	Adjusted transport (Sv)	Reference
A10 (2003)								
Brazil basin	45-15.3°W	Bottom	12:63	9:11	6.9 ± 1.8	2.4	4.2 ± 1.8	(Hogg & Owens, 1999)
Vema channel	39.7-37.7°W	AABW	21:25	9:11	4.0 ± 0.4	1.3	3.8 ± 0.4	(Hogg et al., 1982)
Walvis R. North	7.3°W-1.7°E	Bottom	75:87	9:11	0 ± 1	0.3	-0.4 ± 0.9	(Warren & Speer, 1991)
Walvis R. South	2.2-13.4°E	Bottom	88:106	9:11	0 ± 1	1.2	-0.8 ± 1.3	(Warren & Speer, 1991)
Brazil current	Coast-44.8°W	Surf - interm	1:12	1:7	-38.9 ± 2.1	-21.7	-38.2 ± 1.3	(Hernández-Guerra et al., 2019)
Benguela current	Coast-11.8°E	Surf - interm	101:110	1:7	26.3 ± 2.4	27.8	26.3 ± 1.5	(Hernández-Guerra et al., 2019)
A095 (2009)								
Brazil current	Coast-38.8°W	< 300 dbar	1:4	1:4	-4.9 ± 1.2	-3.1	-3.5 ± 0.2	(Bryden et al., 2011)
A05 + Florida (2004)								
Florida Current	All	All	1:8	1:6	31.9 ± 3.3	31.9	32.2 ± 0.3	Florida Current Project
A03 (2005)								
DWBC	Coast to 70°W	γn 27.8-28.125	1:9	7:9	-25.1 ± 2.7	2.8	-23.4 ± 0.1	(Toole et al., 2011)
AR07W (2005)								
Bering Strait (Davis Strait)	All	All	1:25	1:11	-1.6 ± 0.2	-6.4	-1.6 ± 1.3	(Curry et al., 2014)
AR07E (2007)								
Bering Strait (East)	All	All	26:66	1:11	0.80 ± 0.63	0.1	0.7 ± 2.9	(Lozier et al., 2019)

Table S5. Regional constraints applied to each section for the 2010-19 inverse model. The sixth column represents the imposed value in the model; the seventh column is the mass transport before the model, and the eighth column is the value after the inverse model. The uncertainties for the mass transport adjusted with the inverse model (eighth column) are part of the results of the inverse model using the Gauss-Markov estimator.

Salt constraints	Long	Depth	Stations	Layers	Constraint value (10^{-3} Sv psu)	Initial transport (10^{-3} Sv psu)	Adjusted transport (10^{-3} Sv psu)	Reference
A10 (2011) Bering Strait	All	All	1:119	1:11	-26 ± 21	888	-26 ± 8	(McDonagh et al., 2015)
A095 (2018) Bering Strait	All	All	1:116	1:11	-26 ± 21	1061	-23 ± 8	(McDonagh et al., 2015)
A05 + Florida (2011) Bering Strait	All	All	1:151	1:11	-26 ± 21	911	-24 ± 7	(McDonagh et al., 2015)
A02 (2013) Bering Strait	All	All	1:38	1:11	-26 ± 23	110	-25 ± 7	(McDonagh et al., 2015)
A07 = AR07W + AR07E Bering Strait (total)	All	All	1:80	1:11	-26 ± 23	89	-26 ± 6	(McDonagh et al., 2015)

Table S5 (cont)

Mass constraints	Longitude	Depth	Stations	Layers	Constraint value (Sv)	Initial transport (Sv)	Adjusted transport (Sv)	Reference
A10 (2011)								
Brazil basin	45-15.3°W	Bottom	10:65	9:11	6.9 ± 1.8	4.7	4.8 ± 1.9	(Hogg & Owens, 1999)
Vema channel	39.7-37.7°W	AABW	22:28	9:11	4.0 ± 0.4	2.5	3.9 ± 0.4	(Hogg et al., 1982)
Walvis R. North	7.3°W-1.7°E	Bottom	76:92	9:11	0 ± 1	0.6	-0.4 ± 0.9	(Warren & Speer, 1991)
Walvis R. South	2.2-13.4°E	Bottom	93:116	9:11	0 ± 1	1.1	-0.8 ± 1.2	(Warren & Speer, 1991)
Brazil current	Coast-44.8°W	Surf - interm	1:25	1:7	-38.9 ± 2.1	-16.9	-38.4 ± 1.5	(Hernández-Guerra et al., 2019)
Benguela current	Coast-11.8°E	Surf - interm	105:119	1:7	26.3 ± 2.4	39.0	26.8 ± 1.6	(Hernández-Guerra et al., 2019)
A095 (2018)								
Brazil current	Coast-38.8W	< 300 dbar	1:4	1:10	-4.9 ± 1.2	-4.0	-5.2 ± 0.6	(Bryden et al., 2011)
A05 + Florida (2011)								
Florida Current	All	All	1:13	1:6	31.3 ± 3.4	30.1	30.1 ± 0.2	Florida Current Project
AR07W (2014)								
Bering Strait (Davis Strait)	All	All	1:39	1:11	-1.6 ± 0.2	1.0	-1.6 ± 1.5	(Curry et al., 2014)
AR07E (2014)								
Bering Strait (East)	All	All	40:141	1:11	0.80 ± 0.63	1.3	0.7 ± 2.4	(Lozier et al., 2019)

Table S6. Sensitivity tests for the constraints applied to the South Atlantic in sections A10 (30°S) and A11 (55°S) for regional mass transports. The original inverse model includes these constraints and the inverse model T1 is not constrained by regional and topographic features at 30°S and 55°S. The uncertainties associated with the mass and property transports are part of the results of the inverse model using the Gauss-Markov estimator.

Mass Transport (Sv)		1990-99	2000-09	2010-19
Argentine Basin (55°S)	Original	5.9 ± 1.6		
	T1	2.3 ± 2.8		
Brazil Basin (30°S)	Original	4.4 ± 1.7	4.2 ± 1.8	4.8 ± 1.9
	T1	-0.4 ± 2.1	-1.2 ± 2.3	-0.7 ± 2.5
Vema Channel (30°S)	Original	3.8 ± 0.4	3.8 ± 0.4	3.9 ± 0.4
	T1	1.5 ± 0.9	1.2 ± 0.9	2.0 ± 0.8

		1990-99		2000-09		2010-19	
		Heat (PW)	Freshwater (Sv)	Heat (PW)	Freshwater (Sv)	Heat (PW)	Freshwater (Sv)
Total	Original	0.37 ± 0.06	0.28 ± 0.08	0.42 ± 0.06	0.19 ± 0.07	0.49 ± 0.07	0.09 ± 0.06
	T1	0.43 ± 0.06	0.28 ± 0.08	0.49 ± 0.06	0.19 ± 0.07	0.58 ± 0.07	0.09 ± 0.06
Throughflow	Original	0.01 ± 0.05	0.04 ± 0.05	0.01 ± 0.05	0.04 ± 0.05	0.01 ± 0.06	0.05 ± 0.05
	T1	0.01 ± 0.05	0.04 ± 0.05	0.01 ± 0.06	0.04 ± 0.05	0.01 ± 0.06	0.05 ± 0.05
Overturning	Original	0.49 ± 0.04	0.00 ± 0.02	0.54 ± 0.05	-0.08 ± 0.02	0.60 ± 0.05	-0.13 ± 0.03
	T1	0.54 ± 0.05	0.00 ± 0.02	0.61 ± 0.05	-0.09 ± 0.02	0.69 ± 0.06	-0.13 ± 0.03
Horizontal (gyre)	Original	-0.12 ± 0.01	0.24 ± 0.02	-0.12 ± 0.01	0.23 ± 0.02	-0.11 ± 0.01	0.17 ± 0.01
	T1	-0.12 ± 0.01	0.25 ± 0.02	-0.12 ± 0.01	0.23 ± 0.02	-0.11 ± 0.01	0.17 ± 0.01

Table S7. Sensitivity tests for the values of transport and average salinity of Bering Strait. The results are focused on the heat and freshwater components on the section A10 (30°S). Sensitivity test T2 changes the average salinity of the Bering Strait from 32.5 to 31.5 and T3 to 33.5. Sensitivity test T4 changes the mass transport through Bering Strait from -0.8 ± 0.6 to -1.0 ± 0.5 Sv. The uncertainties associated with the property transports are part of the results of the inverse model using the Gauss-Markov estimator.

		1990-99		2000-09		2010-19	
		Heat (PW)	Freshwater (Sv)	Heat (PW)	Freshwater (Sv)	Heat (PW)	Freshwater (Sv)
Total	Original	0.37 ± 0.06	0.28 ± 0.08	0.42 ± 0.06	0.19 ± 0.07	0.49 ± 0.07	0.09 ± 0.06
	T2	0.37 ± 0.06	0.29 ± 0.10	0.42 ± 0.06	0.20 ± 0.09	0.48 ± 0.07	0.17 ± 0.08
	T3	0.37 ± 0.06	0.26 ± 0.05	0.42 ± 0.06	0.17 ± 0.05	0.48 ± 0.07	0.09 ± 0.04
	T4	0.37 ± 0.06	0.29 ± 0.08	0.42 ± 0.06	0.20 ± 0.07	0.49 ± 0.07	0.10 ± 0.06
Throughflow	Original	0.01 ± 0.05	0.04 ± 0.05	0.01 ± 0.05	0.04 ± 0.05	0.01 ± 0.06	0.05 ± 0.05
	T2	0.01 ± 0.05	0.05 ± 0.08	0.01 ± 0.05	0.06 ± 0.08	0.02 ± 0.06	0.13 ± 0.07
	T3	0.01 ± 0.05	0.02 ± 0.03	0.01 ± 0.05	0.03 ± 0.03	0.02 ± 0.06	0.05 ± 0.03
	T4	0.01 ± 0.05	0.05 ± 0.05	0.01 ± 0.05	0.06 ± 0.05	0.02 ± 0.06	0.06 ± 0.05
Overturning	Original	0.49 ± 0.04	0.00 ± 0.02	0.54 ± 0.05	-0.08 ± 0.02	0.60 ± 0.05	-0.13 ± 0.03
	T2	0.49 ± 0.04	0.00 ± 0.02	0.54 ± 0.05	-0.08 ± 0.02	0.60 ± 0.05	-0.13 ± 0.03
	T3	0.49 ± 0.04	0.00 ± 0.02	0.54 ± 0.05	-0.08 ± 0.02	0.60 ± 0.05	-0.13 ± 0.03
	T4	0.49 ± 0.04	0.00 ± 0.02	0.54 ± 0.05	-0.08 ± 0.02	0.60 ± 0.05	-0.13 ± 0.03
Horizontal (gyre)	Original	-0.12 ± 0.01	0.24 ± 0.02	-0.12 ± 0.01	0.23 ± 0.02	-0.11 ± 0.01	0.17 ± 0.01
	T2	-0.12 ± 0.01	0.24 ± 0.02	-0.12 ± 0.01	0.23 ± 0.02	-0.13 ± 0.03	0.17 ± 0.01
	T3	-0.12 ± 0.01	0.24 ± 0.02	-0.12 ± 0.01	0.23 ± 0.02	-0.11 ± 0.01	0.17 ± 0.01
	T4	-0.12 ± 0.01	0.24 ± 0.02	-0.12 ± 0.01	0.23 ± 0.02	-0.13 ± 0.03	0.17 ± 0.01